Geochronological, isotopic and mineral geochemical constraints on the genesis of the Diyanqinamu Mo deposit, Inner Mongolia, China

Hairui Sun [a,b], Zhilong Huang [a,*], Wenbo Li [c], Lin Ye [a], Jiaxi Zhou [a]

[a] State Key Laboratory of Ore Deposit Geochemistry, Institute of Geochemistry, Chinese Academy of Sciences, Guiyang 550002, China
[b] University of Chinese Academy of Sciences, Beijing 100049, China
[c] Key Laboratory of Orogenic Belt and Crustal Evolution, Peking University, Beijing 100871, China

ABSTRACT

The Diyanqinamu Mo deposit, located in central Inner Mongolia in China, is a newly discovered Mo deposit. Due to the lack of detailed deposit-scale studies, the metallogenesis of the deposit has been a matter of debate. In this study, petrography, zircon U–Pb geochronology, Sr, Nd and Pb isotopes, and apatite mineral geochemistry have been used to constrain the genesis of the Diyanqinamu Mo deposit.
Petrographic evidence indicates that the granites in the Diyanqinamu deposit have experienced fluid exsolution, as demonstrated by the corroded quartz in the porphyritic granites, skeletal quartz in the aplitic granites, and the unidirectional solidification texture (UST) in the apex of the aplitic granites. Sr and Nd isotopic data of the purple fluorite from the fluorite $\pm$ molybdenite veins, showing the $(^{87}Sr/^{86}Sr)_i$ (0.7046–0.7052, avg. 0.7048) and $\varepsilon Nd(t)$ values (2.4–3.8, avg. 3.3) are similar to those of the porphyritic- and aplitic granites. This similarity implies that the Mo ore-forming fluids may have been derived from the granitic magmas. The hypothesis is further supported by the fluorine content (3.79–5.48 wt.%, avg. 4.53 wt.%) in apatite from the porphyritic granites and the widely distributed fluorite in the hydrothermal alteration mineral assemblages, which indicate that the porphyritic granites contain high F content and the hydrothermal fluids are also F-rich. Petrographic observation also shows that magnetite occurs commonly in the hydrothermal mineral assemblages, indicating that the hydrothermal fluids are characterized by high oxygen fugacity (fO_2). It is important to note that the intruding granites are essentially barren, and the Mo is mainly hosted in the andesite and volcaniclastic rocks. In comparison, Pb isotopic compositions of molybdenite are similar to those of both the andesite and K-feldspar from the porphyritic granites, which suggests that both the intruding granites and ore-hosting andesite have contributed to the ore-forming materials. This hypothesis is further supported by the abnormally high Mo for the andesite. Our new evidence suggests that the Diyanqinamu Mo deposit may have formed in a post-collisional extensional environment. Ore-forming materials may have been derived mainly from the granites and minimally from the host rocks. The ore fluids are characterized by high fO_2 and being F-rich, and the trigger for the Mo mineralization has been attributed to the reduction of fO_2 and/or temperature for the ore fluids.

1. Introduction

Diyanqinamu is a newly discovered Mo deposit located in the northern-central part of the Great Xing'an Range. Ore bodies are mainly concentrated in andesite and volcaniclastic rocks (Nie and Hou, 2010; Shandong Gold Group Co. Ltd., 2012; Yan et al., 2012), whereas the granites (including porphyritic- and aplitic granites) intersected in drill holes are essentially barren. Based on zircon U–Pb data, the granites were emplaced at ~156 Ma, which is largely coeval with the Mo mineralization (molybdenite Re–Os: ~156 Ma) (Leng et al., accepted for publication). Therefore, Leng et al. (accepted for publication) speculated that the granite emplacement and Mo mineralization have occurred at

similar time and this deposit could be classified as a porphyry Mo deposit. However, Shao et al. (2011) suggested that this deposit may be classified as a volcanic–subvolcanic hydrothermal deposit according to the concentration of Mo ore bodies in the volcanic and volcaniclastic rocks. The debate on the genesis of the Diyanqinamu Mo deposit is due to the lack of detailed deposit-scale studies including the source(s) of ore-forming materials, the metallogenic mechanism, and the metallogenic role of the ore-hosting andesite and volcaniclastic rocks. In addition, fluorite alteration is widespread at Diyanqinamu and varies in both color and paragenetic minerals. Nevertheless, the fluorites paragenetic with molybdenite are mostly purple, which probably hosts important genetic information but is rarely studied in the past. Furthermore, it is necessary to emphasize that the Diyanqinamu Mo deposit is the only Mo deposit in this region which is characterized by widespread Pb–Zn mineralization and minor Cu or Ag–(Au) mineralization, and

* Corresponding author. Tel.: +86 851 5895900; fax: +86 851 5891664.
E-mail address: huangzhilong@vip.gyig.ac.cn (Z. Huang).

thus studying the Diyanqinamu Mo deposit is also valuable for regional mineral resource exploration.

Geochronology and isotope and mineral geochemistry provide important insights into the genesis of the Diyanqinamu deposit. Zircon, a common accessory mineral in granitoids, is extremely resistant to subsequent geological events and can survive post-crystallization thermal disturbances (Elburg, 1996; Kröner and Liu, 2012). Zircon U–Pb dating of the ore-hosting andesite is carried out for the first time to investigate the metallogenic role of andesite. Sr and Nd isotopes of fluorite (Barker et al., 2009; Bau et al., 2003; Castorina et al., 2008; Halliday et al., 1990; Huang et al., 2007; Jiang et al., 2006; Kinnaird et al., 2004; Sanchez et al., 2010; Sun et al., 2010) and Pb isotope systematics (Carr et al., 1995; Zhou et al., 2001, 2013) are investigated to enable better constraints on the potential source(s) of hydrothermal fluids as well as their migration paths. Fluorine is known to play a significant role in granite petrogenesis and the associated metallogenesis (Candela, 1997; Loferski and Ayuso, 1995; Mountain and Seward, 1999, 2003; Seward and Barnes, 1997). We have investigated the apatite F content because it carries important information on the F concentration in the magmas (Afshooni et al., 2013; Bath et al., 2013; Cao et al., 2014; Icenhower and London, 1997; Munoz, 1984; Nachit et al., 2005).

In this paper, we have mainly focused on the ore deposit geology, zircon U–Pb geochronology, Sr–Nd–Pb isotopes and apatite geochemistry, with the aim to determine the genetic type, magmatic–hydrothermal condition and metallogenic mechanism of the Diyanqinamu Mo deposit.

2. Regional geology

The Diyanqinamu Mo deposit (~120 km NE of Uliastai, northern-central part of the Great Xing'an Range), is situated in the eastern Central Asian Orogenic Belt (CAOB) between the Siberian Craton in the north and the North China Craton in the south (Fig. 1A, B) (Jahn, 2004; Jahn et al., 2000; Li, 2006; Shen et al., 2012). The eastern CAOB has recorded a complex tectonic evolution history including the multiple Paleozoic collisional and suturing episodes between the Siberia- and North China cratons, which has exerted a significant control on the Paleo-Asian tectonics (Chen et al., 2007; Xiao et al., 2003).

These Paleozoic structures were successively overprinted by a prolonged complex tectonics of the Mongolia–Okhotsk Ocean tectonic domain (Meng, 2003; Xu et al., 2013; Ying et al., 2010) and/or the Circum-Paleo-Pacific Ocean tectonic domain (Jiang and Quan, 1988;
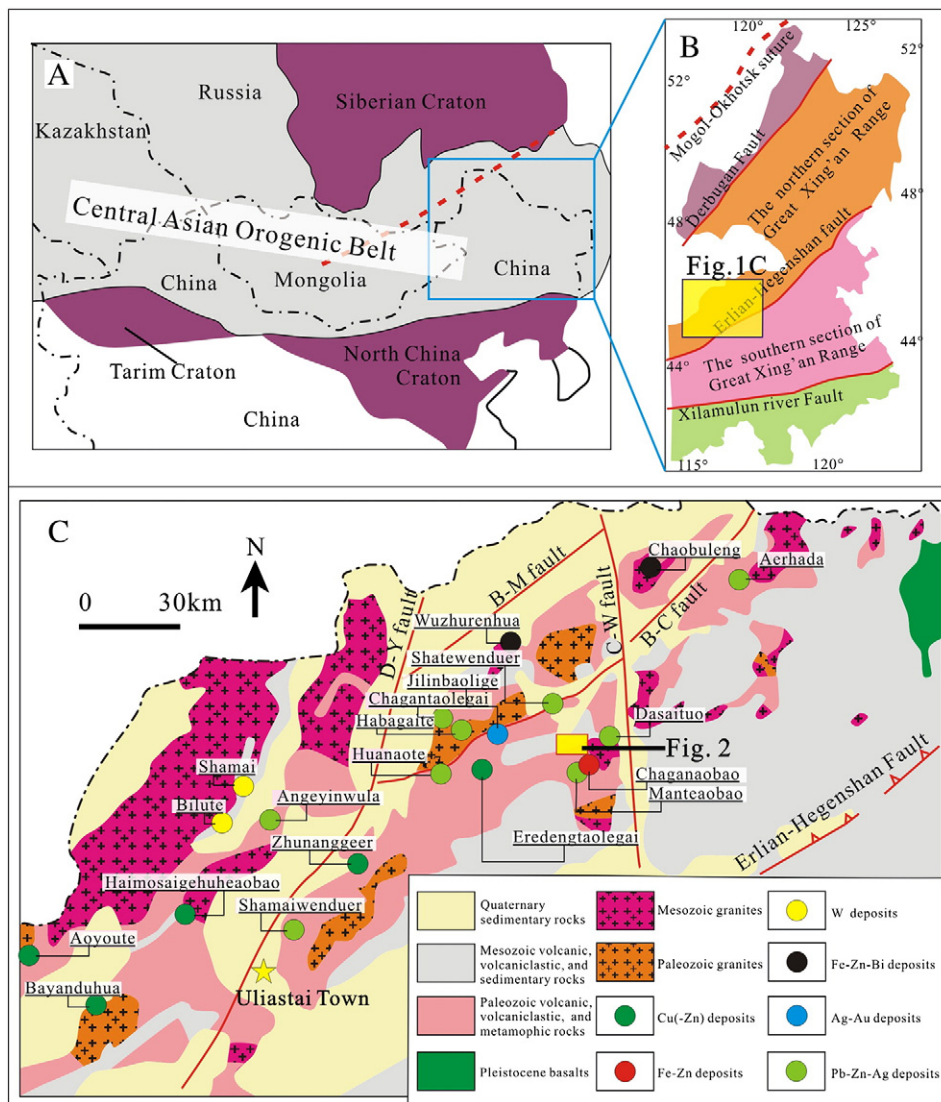

Fig. 1. Simplified regional geological map (A and B) and regional ore deposit map (C) of the Dong–Ujimqin Area (modified after Li, 2006; Shen et al., 2012; Sun et al., 2014; Wang et al., 2009; Zhang et al., 2009). Fault abbreviations: D–Y fault refers to Dong–Ujimqin–Yiheshabaer Fault; B–M fault refers to the Baiyinhubuer–Mandubaolage Fault; B–C fault refers to the Barunshabaer–northern Chaobuleng Fault; C–W fault refers to the Chaobuleng–Wulagai Fault.

Zhang et al., 2010, 2011) since the Mesozoic. The Mongol–Okhotsk domain in the northern Great Xing'an Range marks the suture between the Siberia and North China cratons (Sengör and Natal'in, 1996). This suture is considered to have been formed by the closure of the Mongol–Okhotsk Ocean at the beginning of the Triassic (Zonenshain et al., 1990). Metelkin et al. (2007, 2010) and Tomurtogoo et al. (2005) suggested that the closure of the Mongol–Okhotsk Ocean, which proceeded in a scissor-like fashion from west to east, was completed in eastern Mongolia and Siberia in the Jurassic–early Cretaceous. After the closure of the Mongol–Okhotsk Ocean and the subsequent orogenic collapse, regional tectonic activities were dominated by extensional structures (Meng, 2003; Wang et al., 2006), triggering the formation of basin and range tectonics and voluminous calc-alkaline magmatism, similar to the Basin and Range Province in northwestern America (Fan et al., 2003; Guo et al., 2010). Orogenic collapse related to the Mongol–Okhotsk orogenic belt is also considered to be responsible for the granitic magmatism at Diyanqinamu (Sun et al., 2014).

During the Late Mesozoic, the Mongol–Okhotsk tectonic regime was partially overprinted by the Paleo-Pacific tectonic regime (Xu et al., 2013), which resulted from the subduction of the Paleo-Pacific plate beneath Eurasia (Maruyama and Send, 1986). The subduction was accompanied by voluminous igneous rock emplacement (J.H. Zhang et al., 2008; L.C. Zhang et al., 2008; Wu et al., 2005; Zhang et al., 2011), widespread rifting (Ren et al., 2002) and the formation of the Circum-Paleo Pacific Orogenic Belt (Isozaki et al., 2010; Utsunomiya et al., 2008; Wu et al., 2007; Zhou et al., 2009).

The basement rocks are exposed discontinuously in the region, and consist mainly of Paleozoic and Mesozoic rocks (Fig. 1C), whereas Precambrian is largely absent (Xue et al., 2009). Major components for Paleozoic lithologies are volcanic, volcaniclastic and sedimentary rocks (Nie et al., 2007). The Ordovician is represented by andesite, tuff, andesitic porphyrite and rhyolite interbedded with tuffaceous fine sandstone, tuffaceous slate, siltstone and limestone. The overlying Devonian consists of sandstone and tuffaceous slate, which are overlain by Carboniferous sandstone containing plant fossils and volcanic lava lithic fragments. Permian rocks are composed of andesitic lava, and tuffaceous- and dacitic clastic rocks with interlayers of bioclastic limestone. Triassic rocks are absent in this region. Jurassic rocks overlie uncomfortably the Permian, comprise dominantly volcaniclastic layers of variable thickness, and also contain some intercalated mafic volcanic and sedimentary rocks. The Cretaceous rocks consist mainly of sedimentary rocks such as sandstone, mudstone and conglomerate with interlayers of lignite. NE- and NNE-trending faults are developed in this region with older faults being crosscut by younger ones. Paleozoic and Mesozoic calc-alkaline and A-type granites (Wu et al., 2011; Zhang et al., 2010) are widespread in this region, and part of them are considered to be closely related to various mineral resources (Fig. 1C) (Hong et al., 2003; J. H. Zhang et al., 2008; Nie et al., 2004).

3. Ore deposit geology

At Diyanqinamu, the rocks mainly comprise volcanic, volcaniclastic rocks and weakly metamorphosed types uncomfortably overlain by Quaternary sediments. These volcanic and volcaniclastic rocks (including andesite, rhyolite, dacite, tuff and tuffaceous sandstone) are concentrated at the center of Diyanqinamu (Fig. 2), and have been proposed to be components of the Chagannuoer Formation emplaced in the Late Jurassic (Li et al., 2012; Shao et al., 2011; Yan et al., 2012), although little precise geochronological work is present to support this hypothesis. Besides volcanic and volcaniclastic rocks, weakly metamorphosed rocks, including tuffaceous slate interlayered with tuffaceous sandstone, marble and quartzite, are distributed in the northern part of this deposit, and are classified to be components of the Duobaoshan Formation emplaced in the Middle Ordovician (Yan et al., 2012; Zhang et al., 2009).

The Diyanqinamu area was subjected to intensive tectonic and magmatic activities. Various kinds of faults (including transcurrent and normal faults) trending predominantly NW and NE are the major structures in this deposit (Fig. 2). These structures play an important role in controlling the morphology of the ore bodies. Intrusive bodies include porphyritic granites (as discovered in the drill hole ZK9701) and the crosscutting aplitic granites (as found in the drill holes ZK4522 and ZKp2104). These granites are located in the southeastern quadrant of the Diyanqinamu deposit, and are found intruding into the ore-hosting volcanic and volcaniclastic rocks (Fig. 2). Both the porphyritic- and aplitic granites are high-K calc-alkaline and highly fractionated I-type granites, and are emplaced in the Late Jurassic (zircon U–Pb: ~156 Ma) (Sun et al., 2014). The porphyritic granites in the drill hole ZK9701 are shown at >504 m depth, and consist of quartz (ca. 30%), K-feldspar (ca. 35%), plagioclase (ca. 27%) and biotite (ca. 5%), with minor (ca. 3%) magnetite, zircon and apatite. The aplitic granites
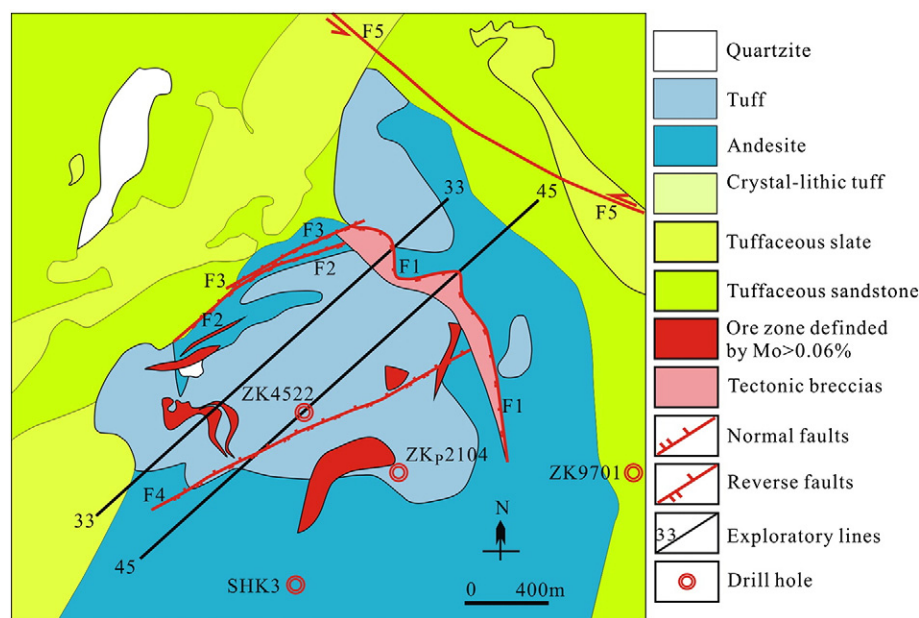

Fig. 2. Simplified geological map of the Diyanqinamu porphyry Mo deposit.
Modified from the unpublished map provided by the Shandong Gold Group Co. Ltd. (2012).

contain relatively fewer K-feldspar and quartz phenocrysts compared with the porphyritic granites. Previous geochronological and geochemical studies indicated a fractional crystallization relationship from the porphyritic- to aplitic granites at Diyanqinamu (Sun et al., 2014). Quartz in the porphyritic granites is rounded and displays distinct corroded texture (Fig. 3A, B), whereas the aplitic granites are characterized by widespread occurrence of skeletal quartz (Fig. 3C, D). Particularly, unidirectional solidification texture (UST, Fig. 3E, F) is observed in drill hole ZK4522 at the apex of the aplitic granites.

Based on the near-infrared spectroscopy and XRD analyses, Yan et al. (2012) and Leng et al. (accepted for publication) have recognized that propylitic, phyllic and argillic alterations were the main hydrothermal alteration types, and that propylitic alteration zone is developed around major Mo ore bodies. In addition, fluorite alteration is found to be another important alteration type, and shows a wide variety of colors including purple, green and white.

Molybdenum is the only economic metal resources at Diyanqinamu, containing proven Mo reserves of 0.79 Mt (average grade: 0.099%). As a whole, ore bodies display a flattened circular shape at different elevations with long axis extending northeastward (Fig. 4A). Most of them are hosted in the Diyanqinamu andesite and volcaniclastic rocks, and are located above 400 m elevation, whereas individual ore body may reach ~250 m elevation in some drill holes such as ZK4111 and

ZK4522 (Fig. 4B, C). Molybdenite Re–Os dating indicates that the Mo mineralization occurred at ~156 Ma (Leng et al., accepted for publication). The Mo mineralization occurs as disseminated grains, banded, fracture infills and veins (Fig. 5A–I). Major ore minerals are pyrite and molybdenite, and minor ore minerals are chalcopyrite, galena, sphalerite, bismuthinite, arsenopyrite and scheelite. Gangue minerals are quartz, feldspar, sericite, fluorite and calcite. It is important to note that the fluorites paragenetic with molybdenite are mostly purple (Fig. 5A, B, C and H), which is particularly obvious in the exploration line 33 (Fig. 4B). Based on field and petrographic observations of the various crosscutting relationships of veins, as well as the paragenetic relationships of various hydrothermal minerals, Leng et al. (accepted for publication) have established five generations of hydrothermal veins. Among them, the magnetite paragenetic with molybdenite in veins occurred at the early stage (Fig. 6A, B and C).

4. Sample selection and analytical methods

4.1. LA-ICP-MS zircon U–Pb dating

Zircon grains were separated from the unaltered ore-hosting andesite collected from the drill hole SHK3. The separated zircon grains were then mounted in epoxy resin and polished to approximately half of their
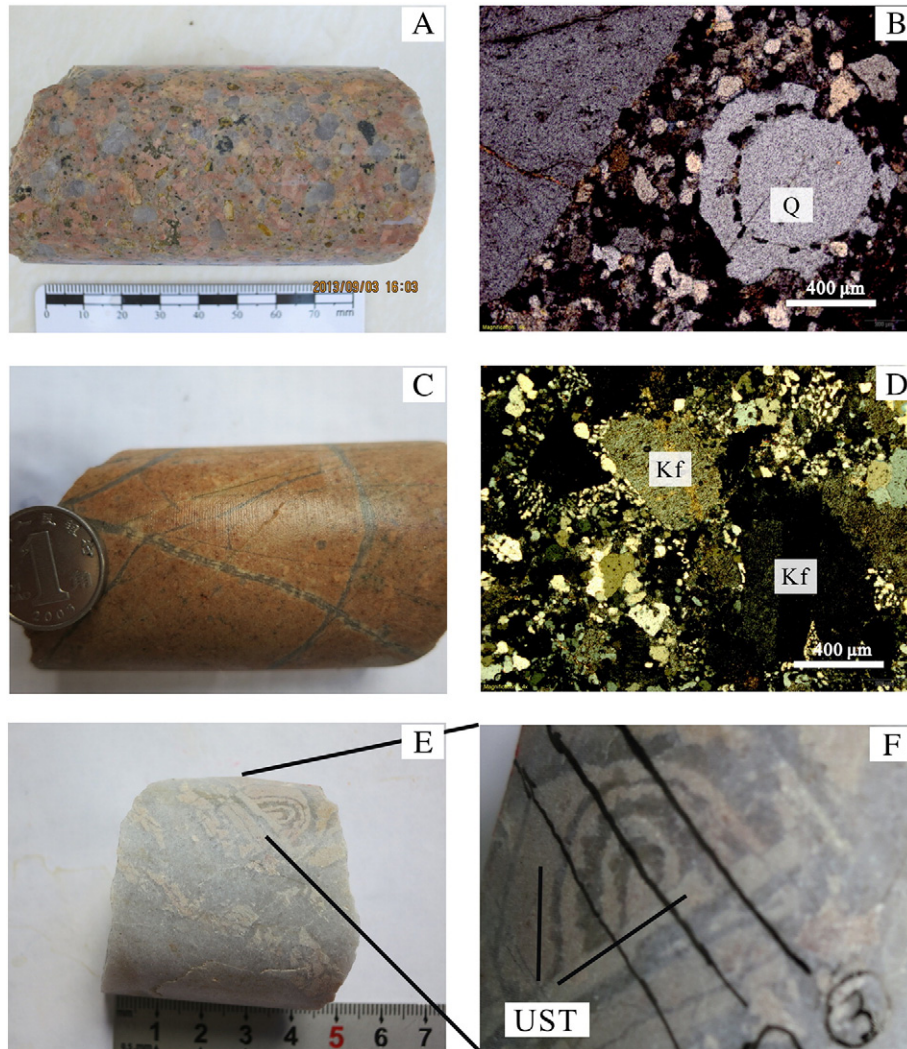

Fig. 3. Photos and photomicrographs of the Diyanqinamu granites. Porphyritic granite in drill hole ZK9701: A—Porphyritic granite; B—quartz phenocrysts displaying corrosion texture. Aplitic granite in drill hole ZKp2104: C—aplitic granite; D—skeletal quartz phenocrysts; E and F—Unidirectional solidification texture (UST) in the apex of the aplitic granite. Mineral abbreviations: Kf—K-feldspar; Q—Quartz.
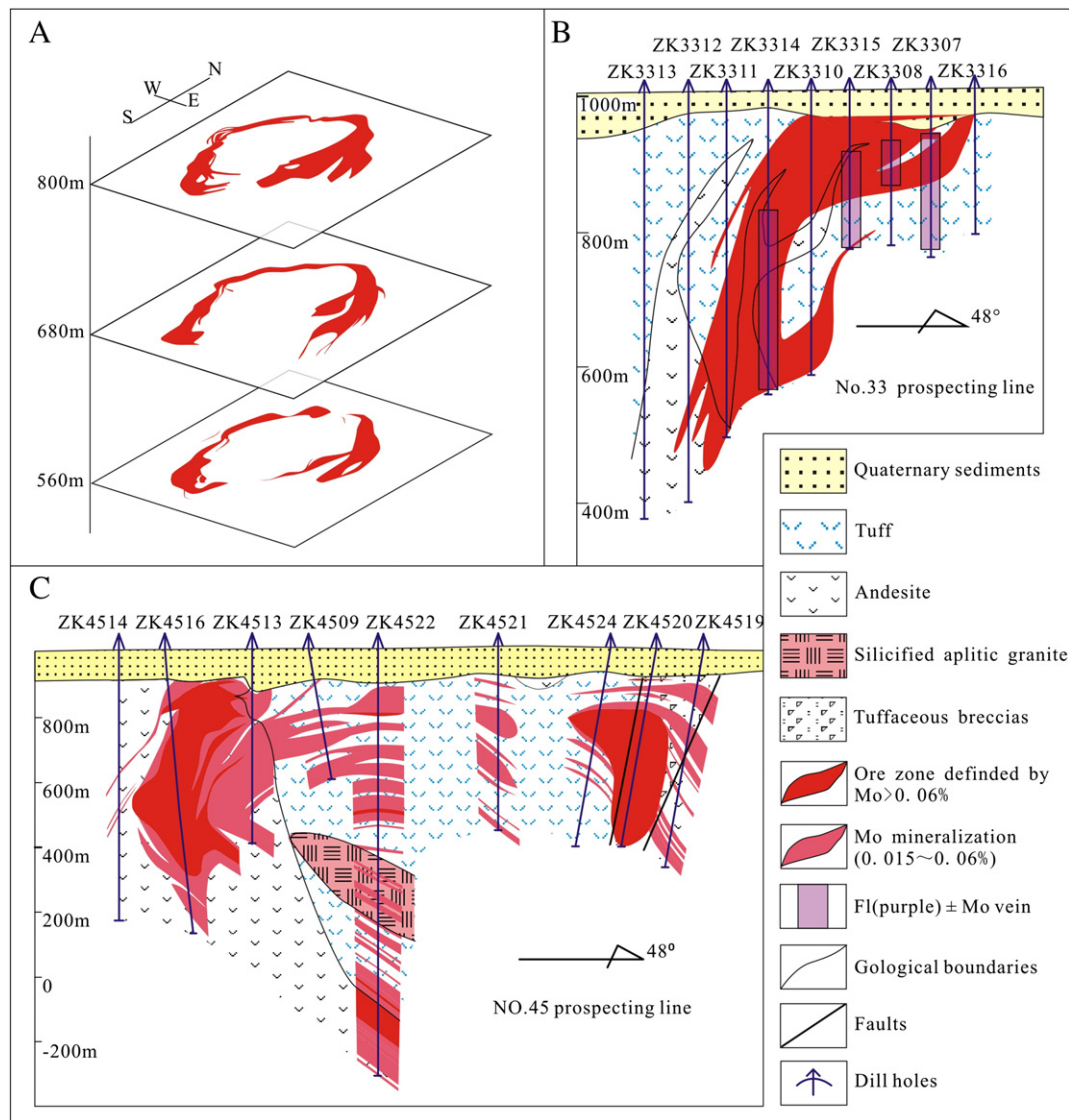
Fig. 4. Three-dimensional morphology of the ore body (A) and geological profile of the exploratory lines (B and C) (modified from unpublished map provided by Shandong Gold Group Co. Ltd. (2012)). Mineral abbreviations: Fl—fluorite; Mo—molybdenite.

thickness. Examination of the internal structure was performed with cathodoluminescence imaging using a scanning electron microscope (SEM) JSM6510 at Beijing Geoanalysis Co., Ltd. Zircon U–Pb dating was conducted using LA-ICP-MS at the State Key Laboratory of Ore Deposit Geochemistry in Guiyang. A GeoLasPro laser-ablation (LA) system (Lamda Physik) and an Agilent 7700× ICP-MS (Agilent Technologies) were combined for the experiment. The 193 nm ArF excimer laser, homogenized by a set of beam delivery systems, was focused on the zircon surface with a fluence of 10 J/cm². According to the grain size of the zircon, the ablation protocol employed spot diameters of 44 μm at 3 Hz repetition rates for 40 s (equating to 120 pulses) for those from the andesite. Helium was applied as a carrier gas to efficiently transport aerosols to the ICP-MS. Zircon 91500 (Wiedenbeck et al., 1995) was used as an external standard to correct instrumental mass discrimination and elemental fractionation. Zircon GJ-1 (Jackson et al., 2004) and Plešovice (Sláma et al., 2008) were treated as quality controls for the geochronology analysis. The Pb abundance of zircon was externally calibrated against the NIST SRM 610 (Baker et al., 2004), using Si as the internal standard, whereas Zr was used as an internal standard for the other trace elements (Hu et al., 2011; Liu et al., 2010b). Raw data calculation was performed offline by the ICPMSDataCal software (Liu et al., 2010a,b).

4.2. Sr, Nd and Pb isotopic analysis

Six purple fluorite samples were collected from the drill holes ZK3314 and ZK2505. These fluorites are paragenetic with molybdenite and selected for Sr and Nd isotopic analyses. Fluorite grains were handpicked under a binocular microscope, and treated with 10% HCl and rinsed with distilled water. After drying at 25–30 °C, the concentrations were grounded. Sr and Nd isotopic measurements were performed with a Thermal Ionization Mass Spectrometry (TIMS) at the State Key Laboratory of Ore Deposit Geochemistry in Guiyang. Triton is the brand name of the TIMS which is made by the Thermo Fisher Scientific of Germany. Analytical procedures for both Sr and Nd isotopic determinations were similar. Samples were dissolved in HF + HClO$_4$. Rb, Sr and REE were separated using AGW50 × 12 cation exchange columns. REE were further dissolved in 0.1 N HCl, then Sm and Nd were separated on the levextrel resin ion exchange columns. ^{87}Rb/^{86}Sr and ^{147}Sm/^{144}Nd ratios analyzed at the laboratory were calculated using the Rb, Sr, Sm and Nd abundances measured by ICP-MS. Several analyses on the NBS-987 Sr standard yielded ^{87}Sr/^{86}Sr = 0.710254 ± 5 (2σ). The mean ^{143}Nd/^{144}Nd ratios for the La Jolla and Jndi-1 Nd standard were 0.511544 ± 3 (2σ) and 0.512104 ± 5 (2σ) respectively. ^{143}Nd/^{144}Nd ratios were normalized to the value of ^{146}Nd/^{144}Nd = 0.7219.
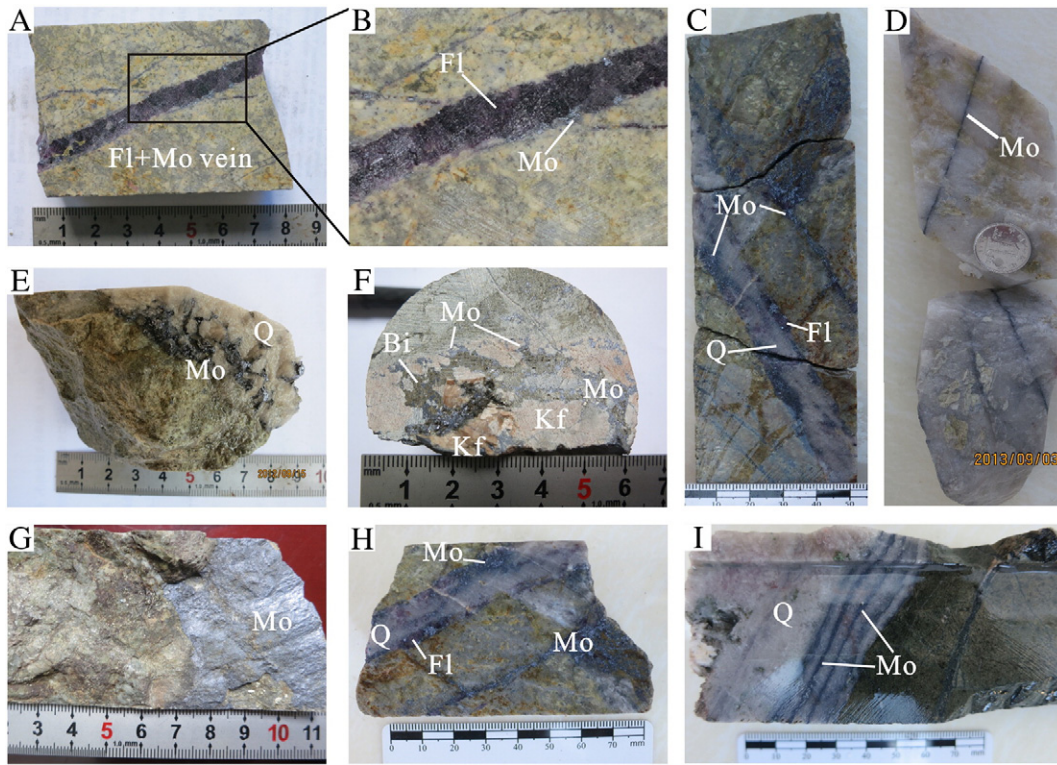
Fig. 5. Photos of mineralized rocks in the Diyanqinamu Mo mine. (A) and (B): Mo ± Fl vein; (C): Q ± Fl ± Mo vein in tuff; (D): molybdenite film in the fracture of quartz vein; (E): disseminated molybdenite in Q ± Mo vein from altered tuff; (F): biotite and molybdenite display interstitial distribution in Kf ± Bi ± Mo vein; (G): molybdenite film in altered tuff; (H): Mo ± Fl ± Q vein in tuff; (I): molybdenite band in molybdenite ± quartz vein which is crosscutting by barren quartz vein. Mineral abbreviations: Bi—biotite. Other abbreviations are the same as in Fig. 4.
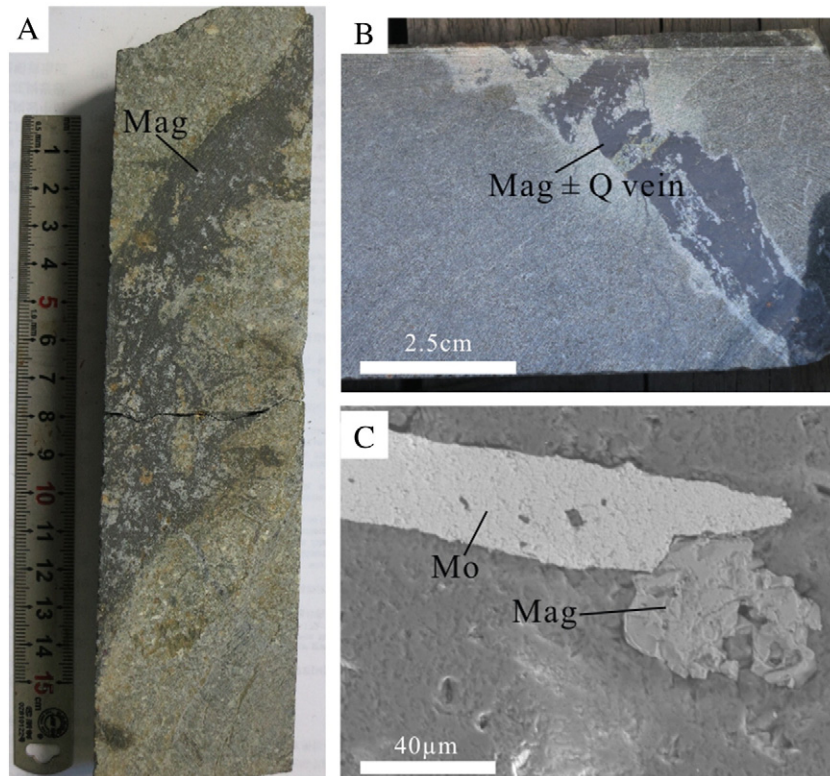

Fig. 6. Photos and photomicrographs of magnetite alteration. (A) and (B): Magnetite ± quartz vein. (C): Magnetite paragenetic with molybdenite in fluorite ± molybdenite ± magnetite vein. Mineral abbreviations: Mag—magnetite. Other abbreviations are the same as in Fig. 4.

Fractionation effects during the Sr isotopic composition runs were eliminated by normalizing to an $^{86}Sr/^{88}Sr$ value of 0.1194.

Nineteen samples (ten molybdenites, four K-feldspar from the porphyritic granites and five andesites) have been analyzed for their Pb isotope composition. The samples of molybdenite and K-feldspar were separated by handpicking under a binocular microscope. Separated grains were rinsed with distilled water. After drying at 25–30 °C, the concentrations were grounded. All the samples were analyzed with a MAT 261 mass spectrometer using the thermal ionization cross-section analytical technique at the Geological Analysis Laboratory under the Ministry of Nuclear Industry in Beijing. The precision of the $^{208}Pb/^{206}Pb$ measurements (1 µg of Pb) is ≤0.005%, and the measured ratios (2σ) of international standard sample NBS981 are $^{208}Pb/^{204}Pb = 36.611 \pm 0.004$, $^{207}Pb/^{204}Pb = 15.457 \pm 0.002$, and $^{206}Pb/^{204}Pb = 16.937 \pm 0.002$, in accordance with the reference value (Belshaw et al., 1998).

4.3. Apatite mineral chemistry

The apatite crystals used for geochemical analyses were separated from the porphyritic granites and are paragenetic with and/or included in K-feldspar, quartz and biotite. All the crystals are acicular or columnar with 30–150 µm in size. Major element composition of apatite was measured at the IGGCAS using an EPMA-1600 electron microprobe of Shimadzu Company operated in wavelength dispersive spectrometers (WDS) mode. The operating conditions were 25 kV accelerating voltage, 10 nA beam current and 10 µm probe beam. The following natural minerals and synthetic oxides were used for the calibration: apatite (P, Ca and F), biotite (Mg, Si and Fe), amphibole (Na and Mn) and tugtupite (Cl).

5. Results

5.1. Zircon U–Pb age of the ore-hosting andesite

Fifteen zircon grains from the unaltered ore-hosting andesite have clear igneous oscillating zonation (Fig. 7A), indicating a magmatic origin. These zircons have U and Th contents of 288 to 1877 ppm and 53 to 693 ppm, respectively (Table 1). Th/U values range from 0.2 to 0.8, which further supported their magmatic origin (Hoskin and Schaltegger, 2003). Three older zircon grains with $^{207}Pb/^{235}U$ ages of 830 Ma (Spot SHK-01), 797 Ma (Spot SHK-03) and 1113 Ma (Spot SHK-04) were detected (Fig. 7B), which may have been either inherited or xenocrystic zircons trapped during the magma generation and/or emplacement. The other 12 of them formed a cluster and yielded a concordia age of 260 ± 4 Ma (Fig. 7C).

5.2. Sr, Nd and Pb isotope composition

The six fluorite samples analyzed have similar Sr and Nd isotopic composition (Table 2). The initial $^{87}Sr/^{86}Sr$ values range from 0.7046 to 0.7052 with an average of 0.7048, and εNd(t) values range from 2.4 to 3.8 with an average of 3.3. The εNd(t) data are similar to those of both porphyritic granites (3.3–3.8, average: 3.6) and aplitic granites (2.4–3.2, average: 2.9) at Diyanqinamu.
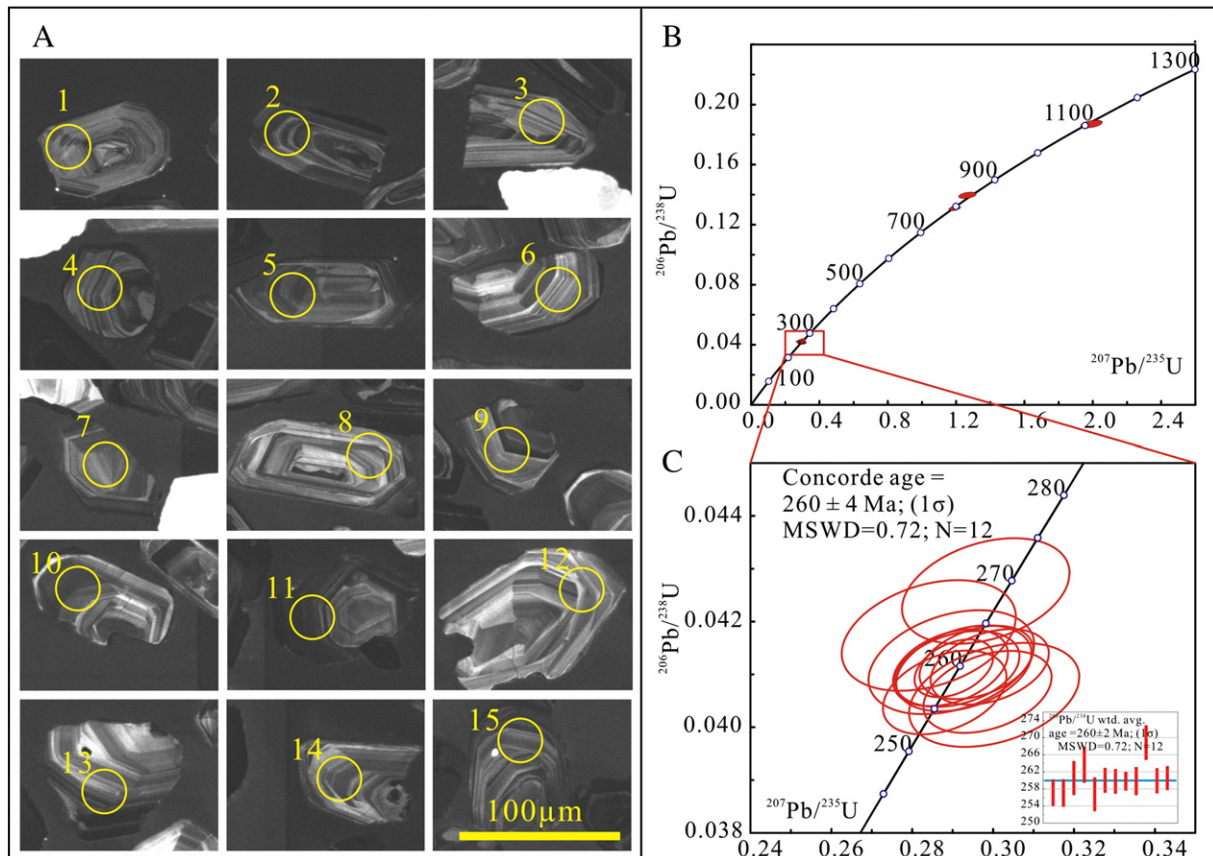

Fig. 7. Cathodoluminescence images of zircon grains (A) and zircon $^{207}Pb/^{235}U$–$^{206}Pb/^{238}U$ concordia plot (B, C) of the ore-hosting andesite.

Table 1
LA-ICP-MS U–Th–Pb analytical zircon data of andesite in the Diyanqinamu deposit.

Spot no.	Pb	Th	U	Th/U	$^{207}Pb/^{206}Pb$		$^{207}Pb/^{235}U$		$^{206}Pb/^{238}U$		$^{207}Pb/^{206}Pb$		$^{207}Pb/^{235}U$		$^{206}Pb/^{238}U$	
	ppm			Ratio	Ratio	1σ	Ratio	1σ	Ratio	1σ	Age (Ma)	1σ	Age (Ma)	1σ	Age (Ma)	1σ
SHK-01	46	53	292	0.18	0.0649	0.00178	1.2656	0.03415	0.1390	0.00142	772	53	830	15	839	8
SHK-02	25	328	515	0.64	0.0531	0.00189	0.2988	0.01040	0.0407	0.00051	345	80	265	8	257	3
SHK-03	86	304	555	0.55	0.0654	0.00130	1.1912	0.02294	0.1303	0.00109	787	41	797	11	790	6
SHK-04	91	210	413	0.51	0.0766	0.00162	1.9921	0.04182	0.1867	0.00174	1110	10	1113	14	1104	9
SHK-05	28	408	572	0.71	0.0517	0.00190	0.2883	0.01007	0.0407	0.00052	272	85	257	8	257	3
SHK-06	15	138	295	0.47	0.0500	0.00223	0.2900	0.01347	0.0412	0.00065	195	104	259	11	261	4
SHK-07	19	244	381	0.64	0.0494	0.00255	0.2844	0.01413	0.0417	0.00069	165	120	254	11	264	4
SHK-08	17	213	321	0.66	0.0533	0.00263	0.3005	0.01385	0.0406	0.00065	343	108	267	11	257	4
SHK-09	32	459	627	0.73	0.0521	0.00174	0.2994	0.00962	0.0412	0.00047	287	76	266	8	260	3
SHK-10	31	448	591	0.76	0.0508	0.00184	0.2914	0.01013	0.0411	0.00047	232	88	260	8	260	3
SHK-11	90	693	1877	0.37	0.0501	0.00114	0.2906	0.00640	0.0411	0.00036	211	54	259	5	260	2
SHK-12	19	300	365	0.82	0.0521	0.00208	0.2930	0.01098	0.0411	0.00053	300	91	261	9	260	3
SHK-13	15	125	288	0.43	0.0506	0.00236	0.2984	0.01359	0.0426	0.00066	220	109	265	11	269	4
SHK-14	24	229	493	0.46	0.0506	0.00171	0.2897	0.00930	0.0411	0.00048	220	78	258	7	260	3
SHK-15	50	467	1033	0.45	0.0510	0.00162	0.2961	0.00921	0.0412	0.00046	243	79	263	7	261	3

Pb isotopic results of K-feldspar, whole rock andesite and molybdenite are listed in Table 3. In comparison, the Pb isotope ratios of K-feldspar and andesite are similar to that of molybdenite in all $^{206}Pb/^{204}Pb$, $^{207}Pb/^{204}Pb$ and $^{208}Pb/^{204}Pb$ ratios.

5.3. Apatite mineral geochemistry

Chemical compositions of the representative apatite grains are listed in Table 4. CaO and P_2O_5 are the main constituents of apatite. CaO content ranges from 52.25 wt.% to 54.75 wt.% with an average of 53.55 wt.% and P_2O_5 content ranges from 39.79 wt.% to 42.90 wt.% with an average of 41.52%. MgO, Na_2O, MnO, SiO_2 and FeO contents are all very low. Fluorine content is very high, ranging from 3.79 wt.% to 5.48 wt.% with an average of 4.54 wt.%, and correlates negatively with the predominantly low to very low Cl (0.01–0.05 wt.%, average: 0.02 wt.%) content.

6. Discussion

6.1. The source of ore-forming materials

Understanding the origin of the ore-forming materials in hydrothermal deposits is essential for establishing the genetic framework of the deposit (Heinrich et al., 1992). Petrographic evidence (Candela, 1997; Seedorff et al., 2005), and Sr–Nd (Halliday et al., 1990) and Pb isotopes (Zartman and Doe, 1981; Zhou et al., 2013) are useful in determining the origin(s) of the ore-forming materials.

At Diyanqinamu, the porphyritic granites are characterized by wide distribution of corroded quartz, which indicates the saturation of magmatic volatile phase because corrosion of quartz may occur when water content of granitic magma is high and vapor phase is saturated. Then, the skeletal quartz in aplitic granites could be attributed to undercooling of this magma which is saturated with magmatic volatile phase (Candela, 1997; Ratajeski, 1995), since geochronological and geochemical studies have demonstrated that the porphyritic granite and aplitic granites were highly fractionated I-type and the aplitic granites were generated by fractional crystallization of the porphyritic one (Sun et al., 2014). It is commonly accepted that the magmatic–hydrothermal transition plays a critical role in the formation of hydrothermal ore deposits (Chang and Meinert, 2004), and UST records the transition from magmatic to hydrothermal conditions, commonly presents in granite-related Mo and Sn–W systems (Lowenstern and Sinclair, 1996), is one of the common features for porphyry deposits (Sinclair, 2007), and demonstrates the local accumulation of aqueous fluids at the apex of aplitic stocks during late fractional crystallization (Seedorff et al., 2005). Then, UST, occurring along the margins of the aplitic granites in the Diyanqinamu deposit (Fig. 3E, F), suggests that the accumulation of aqueous fluids deriving from the granitic melt has occurred.

Table 2
The Sr and Nd isotopic data of porphyritic granite, aplitic granite, and purple fluorites.
The Rb, Sr, Nd, and Sm contents of fluorites are analyzed by ICP-MS at the State Key Laboratory of Ore Deposit Geochemistry in Guiyang. The analysis processes are described in detail by Qi and Gregoire (2000).

Sample no.	Lithology	Rb (ppm)	Sr (ppm)	$^{87}Rb/^{86}Sr$	$^{87}Sr/^{86}Sr$	2σ	$(^{87}Sr/^{86}Sr)_i$	Sm (ppm)	Nd (ppm)	$^{147}Sm/^{144}Nd$	$^{143}Nd/^{144}Nd$	2σ	$(^{143}Nd/^{144}Nd)_i$	εNd(t)	References
P2104-2	Aplitic granite	226	83.8	7.7974	0.718661	16	0.7014	0.96	5.97	0.0970	0.512670	10	0.51257	2.6	Sun et al.
P2104-3		217	64.7	9.7301	0.723698	10	0.7021	1.10	7.37	0.0899	0.512650	6	0.51256	2.4	(2014)
P2104-4		241	58.4	11.9608	0.728055	10	0.7015	1.50	9.56	0.0946	0.512699	10	0.51260	3.2	
P2104-5		247	79.7	8.9543	0.721807	10	0.7019	1.20	7.66	0.0942	0.512698	10	0.51260	3.2	
9701-16	Porphyritic	245	65.0	10.8952	0.727691	12	0.7035	3.78	22.6	0.1006	0.512711	12	0.51261	3.3	Sun et al.
9701-17	granite	259	69.2	10.8328	0.728214	8	0.7042	3.67	21.6	0.1024	0.512725	4	0.51262	3.6	(2014)
9701-18		266	76.5	10.0491	0.724885	16	0.7026	3.08	19.0	0.0978	0.512724	6	0.51262	3.7	
9701-20		277	100	8.0071	0.722037	12	0.7043	3.95	23.4	0.1015	0.512734	8	0.51263	3.8	
9701-21		269	158	4.9148	0.715411	16	0.7045	4.74	26.8	0.1065	0.512733	6	0.51262	3.7	
ZK3314-4	Purple fluorite	1.26	109	0.0334	0.705289	10	0.7052	19.4	53.9	0.2166	0.512844	8	0.51262	3.6	This study
ZK3314-8		2.40	86.9	0.0799	0.704993	8	0.7048	7.19	19.7	0.2196	0.512785	8	0.51256	2.4	This study
ZK3314-19		0.65	78.2	0.0240	0.704763	12	0.7047	5.56	18.2	0.1838	0.512817	6	0.51263	3.8	This study
ZK3314-21		1.85	91.3	0.0586	0.704862	12	0.7047	5.56	18.2	0.1838	0.512785	4	0.51260	3.1	This study
ZK2505-8		2.68	74.4	0.1042	0.704950	14	0.7047	7.19	19.7	0.2196	0.512838	8	0.51261	3.4	This study
ZK2505-10		1.22	73.1	0.0483	0.704685	10	0.7046	11.3	26.4	0.2576	0.512886	4	0.51262	3.6	This study

Note: The age used in this calculation is based on the zircon U–Pb ages of 156 Ma of porphyritic granite and aplitic granites.

Table 3
Lead isotopic composition of K-feldspar, andesite and molybdenite.

Sample no.	Lithology	$(^{206}Pb/^{204}Pb)_{156\ Ma}$	$(^{207}Pb/^{204}Pb)_{156\ Ma}$	$(^{208}Pb/^{204}Pb)_{156\ Ma}$
ZK9701-8	K-feldspar of	18.370	15.547	38.133
ZK9701-9	porphyritic granite	18.352	15.538	38.091
ZK9701-11		18.376	15.556	38.149
ZK9701-12		18.400	15.533	38.130
SHK3-1	Andesite	18.317	15.495	38.005
SHK3-3		18.359	15.468	38.054
SHK3-4		18.307	15.536	38.073
SHK3-6		18.337	15.441	37.992
SHK3-7		18.321	15.431	38.003
ZK6112-5	Molybdenite	18.285	15.502	37.939
PF2702-5		18.290	15.511	37.958
PF2702-7		18.276	15.502	37.936
PF2702-12		18.297	15.532	38.023
PF2702-13		18.307	15.533	38.031
ZK3734-14		18.317	15.529	38.038
ZK3734-16		18.291	15.508	37.950
ZK6115-6		18.304	15.509	37.982
ZK6115-7		18.308	15.514	37.976
ZK6115-9		18.295	15.504	37.949

Note: the Pb isotopic data of andesite are calculated based on the zircon U–Pb age 156 Ma of the granites, whereas the Pb isotopic data of K-feldspar of porphyritic granites and molybedenite in this table are without calculation again. The reduction formula: $(^{206}Pb/^{204}Pb)_t = (^{206}Pb/^{204}Pb)_p - \mu(e^{\lambda t} - 1)$; $(^{207}Pb/^{204}Pb)_t = (^{207}Pb/^{204}Pb)_p - \mu / 137.88(e^{\lambda' t} - 1)$; $(^{208}Pb/^{204}Pb)_t = (^{208}Pb/^{204}Pb)_p - \omega(e^{\lambda'' t} - 1)$; $\lambda = 1.55125 \times 10^{-10}\ t - 1$, $\lambda' = 9.8485 \times 10^{-10}\ t - 1$, $\lambda'' = 0.49475 \times 10^{-10}\ t - 1$; $t = 156$ Ma.

Fluorite alteration is an important feature at Diyanqinamu. The purple fluorites sampled from the fluorite ± molybdenite veins have similar εNd(t) to those of both porphyritic- and aplitic granites (Table 2 and Fig. 8). In comparison, initial $^{87}Sr/^{86}Sr$ values of the fluorites are similar to those of porphyritic granites, but different from those of aplitic granites. This decoupling in initial $^{87}Sr/^{86}Sr$ values may be attributed to the post-magmatic alteration. In the Pb isotope evolution diagrams (Zartman and Doe, 1981), all data points of the molybdenite overlap with those of K-feldspar from the porphyritic granites (Fig. 9). All of them fall between the mantle Pb evolution curve and the orogenic belt evolution curve (Fig. 9), indicating that Pb was mostly derived from the mantle or lower crust with minor supracrustal component. Pb isotope of the molybdenite and K-feldspar also shares similar characteristics with that of the Mesozoic volcanics, showing radiogenic Nd compositions (εNd(t) > 0) in the Great Xing'an Range (Chen et al., 2009; Guo et al., 2010; Sun et al., 2014). Previous studies indicated that these igneous rocks might be formed by partial melting of the preexisting juvenile crust which resembled lithospheric mantle in terms of Nd isotope characteristics (Sun et al., 2014; Wu et al., 2000, 2003). In general, porphyritic granites in porphyry Mo deposits are

Table 4
Electron microprobe analyses in representative apatite from porphyritic granites.

|	No.	CaO	P$_2$O$_5$	MgO	Na$_2$O	MnO	SiO$_2$	FeO	Cl	F	− O≡F,Cl	Total	F$_{melt}$
ZK9701-16	-1	53.77	40.46	0.00	0.23	0.30	0.36	0.05	0.02	4.15	1.75	97.59	0.10–0.38
	-2	53.56	39.89	0.03	0.23	0.27	0.36	0.07	0.02	4.98	2.10	97.30	0.12–0.45
	-3	53.35	39.79	0.02	0.37	0.28	0.41	0.05	0.02	4.69	1.98	96.99	0.12–0.43
	-4	53.04	40.70	0.00	0.23	0.23	0.58	0.08	0.03	4.62	1.95	97.56	0.12–0.42
	-5	53.16	41.15	0.01	0.47	0.25	0.33	0.07	0.04	4.39	1.86	98.01	0.11–0.40
	-6	53.59	41.40	0.01	0.41	0.28	0.35	0.09	0.02	4.49	1.89	98.73	0.11–0.41
	-7	52.72	39.84	0.02	0.27	0.30	0.55	0.06	0.03	4.53	1.91	96.40	0.11–0.41
	-8	53.85	41.03	0.01	0.21	0.41	0.43	0.17	0.03	4.88	2.06	98.97	0.12–0.44
	-9	53.95	42.90	0.00	0.27	0.22	0.20	0.04	0.04	3.95	1.67	99.91	0.10–0.36
	-10	53.93	42.16	0.01	0.24	0.24	0.46	0.04	0.02	4.57	1.93	99.74	0.11–0.42
ZK9701-17	-1	54.07	41.27	0.01	0.21	0.33	0.24	0.16	0.01	4.92	2.07	99.15	0.12–0.45
	-2	53.96	41.47	0.01	0.18	0.42	0.31	0.05	0.01	4.35	1.84	98.93	0.11–0.40
	-3	53.88	41.24	0.00	0.32	0.28	0.26	0.06	0.02	4.64	1.96	98.75	0.12–0.42
	-4	54.75	41.20	0.00	0.17	0.26	0.40	0.04	0.01	4.30	1.81	99.31	0.11–0.39
	-5	52.25	41.00	0.02	1.10	0.29	2.00	0.09	0.01	3.94	1.66	99.03	0.10–0.36
	-6	54.49	42.63	0.01	0.15	0.26	0.22	0.10	0.02	4.45	1.88	100.44	0.11–0.40
	-7	54.06	42.15	0.00	0.34	0.27	0.16	0.08	0.01	4.79	2.02	99.85	0.12–0.44
	-8	54.39	42.26	0.01	0.36	0.28	0.16	0.22	0.01	4.21	1.77	100.12	0.11–0.38
	-9	54.03	42.32	0.01	0.28	0.31	0.22	0.42	0.01	5.48	2.31	100.76	0.14–0.50
	-10	53.43	41.49	0.02	0.20	0.28	0.28	0.10	0.01	4.84	2.04	98.61	0.12–0.44
	-12	53.81	41.71	0.01	0.26	0.30	0.26	0.17	0.01	4.59	1.94	99.19	0.11–0.42
	-13	54.00	41.26	0.01	0.36	0.33	0.21	0.35	0.02	4.63	1.95	99.20	0.12–0.42
ZK9701-18	-1	53.67	41.18	0.02	0.26	0.28	0.45	0.05	0.03	4.48	1.89	98.52	0.11–0.41
	-2	53.47	41.74	0.01	0.28	0.26	0.98	0.07	0.02	4.24	1.79	99.28	0.11–0.39
	-3	52.63	41.39	0.00	0.24	0.25	0.38	0.02	0.01	4.30	1.81	97.40	0.11–0.39
	-4	52.31	40.74	0.02	0.32	0.33	0.82	0.08	0.02	4.65	1.96	97.31	0.12–0.42
	-5	54.07	41.82	0.01	0.35	0.29	0.34	0.06	0.03	4.83	2.04	99.77	0.12–0.44
	-6	53.69	42.86	0.02	0.35	0.99	0.08	0.08	0.02	3.79	1.60	100.28	0.09–0.34
ZK9701-19	-1	53.53	42.66	0.01	0.43	0.60	0.04	0.07	0.05	4.82	2.04	100.18	0.12–0.44
	-2	52.59	41.54	0.02	0.44	0.38	1.28	0.09	0.02	4.46	1.88	98.93	0.11–0.41
	-3	52.73	42.39	0.02	0.25	0.26	0.62	0.07	0.02	3.96	1.67	98.64	0.10–0.36
ZK9701-21	-1	54.57	41.92	0.01	0.30	0.19	0.20	0.16	0.02	5.12	2.16	100.32	0.13–0.47
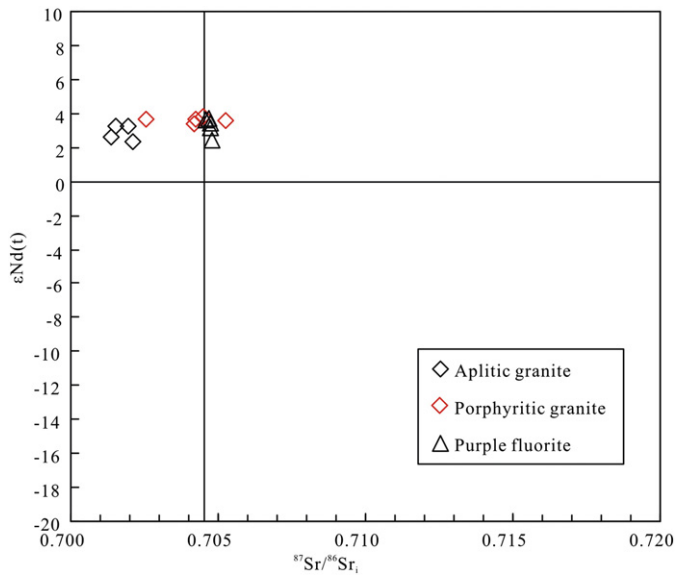
Fig. 8. $(^{87}Sr/^{86}Sr)_i$ vs. $\varepsilon Nd(t)$ diagram of aplitic granite, porphyritic granite and purple fluorite from purple fluorite ± molybdenite veins.
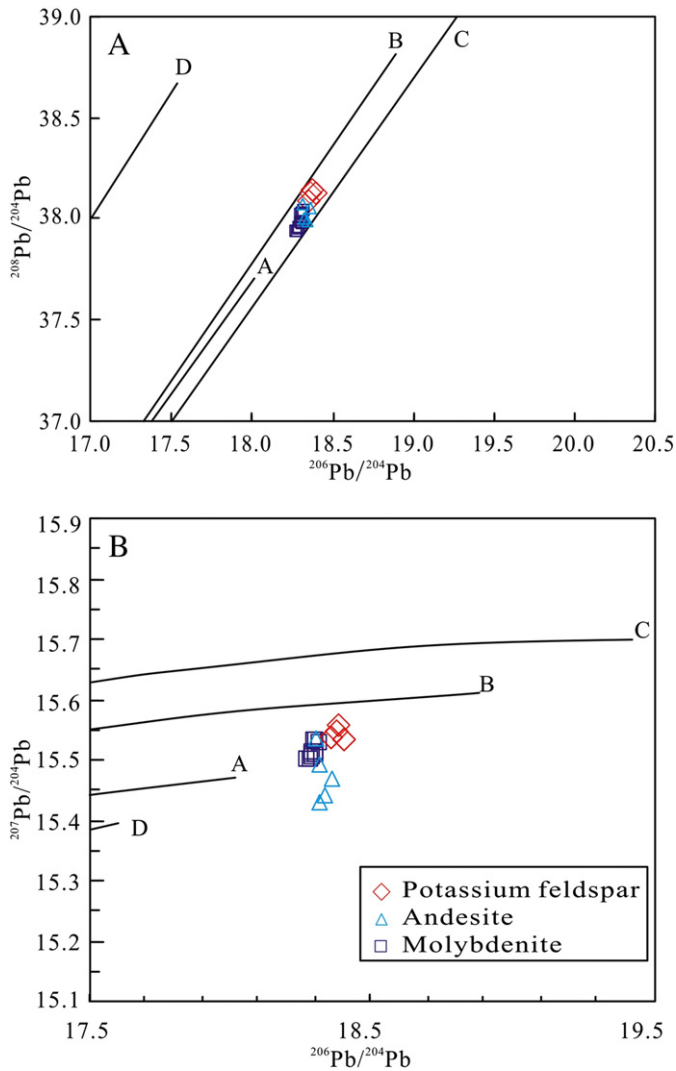

Fig. 9. (A) $^{206}Pb/^{204}Pb$ vs. $^{208}Pb/^{204}Pb$ and (B) $^{206}Pb/^{204}Pb$ vs. $^{207}Pb/^{204}Pb$ plots of K-feldspar from porphyritic granites, andesite, and molybdenite at Diyanqinamu (Zartman and Doe, 1981).

mostly formed by partial melting of the lower crust (White et al., 1981), especially for the deposits that occurred on continents (Hou and Yang, 2009). Then, Pb isotope evidence in this deposit further implies that the sources of ore-forming materials are mainly derived from the lower crust. Therefore, comprehensive evidence of petrography, Sr and Nd isotopic composition of purple fluorites, and Pb isotopic features of the K-feldspar and molybdenite indicate that the ore-forming materials may have come from these granitic magma.

However, all ore bodies discovered so far are hosted in the andesite and volcaniclastic rocks, leading to the question on the role they played during the Mo mineralization. The andesite was emplaced at 260 ± 4 Ma (Fig. 7), which is far older than the Mo mineralization (~156 Ma, Leng et al., accepted for publication). This discordance suggests that the andesitic volcanism has not contributed heat energy to the Mo mineralization. Pb isotope characteristics of the ore-hosting andesite are similar to those of the molybdenite (Fig. 9), indicating a common source. As a result, the andesite is also an important ore-forming material source for the Mo mineralization. This hypothesis is further supported by the fact that the unaltered andesite at Diyanqinamu contains much higher Mo content (up to 32.9 ppm, Table 5) compared with typical andesite around the world (http://georoc.mpch-mainz.gwdg.de/georoc/Start.asp).

A review of global Mo deposits by Cooke et al. (2005) and Sinclair (2007) showed that 95% of the deposits were genetically associated with porphyries. Huang (2007) suggested that 94% of the Mo deposits in China were genetically related to porphyries. There is a consensus that most of the ore-forming fluids and metals in porphyry ore deposits are derived from large intermediate to felsic magma chambers (Halter et al., 2002, 2005; Pettke et al., 2010; Williams-Jones and Heinrich, 2005), together with minor wall rocks (Wu et al., 2010). As a consequence, both the granites and andesite at Diyanqinamu are ore-forming material sources for the Mo mineralization and the Diyanqinamu Mo deposit is best classified as a porphyry Mo deposit.

6.2. Characteristics of the magmatic–hydrothermal system and their metallogenic significance

6.2.1. Oxidized magmatic–hydrothermal system and its metallogenic significance

It is generally believed that porphyry Cu–(Mo–Au) ore fluids are relatively oxidized (Afshooni et al., 2013; Burnham and Ohmoto, 1980; Rowins, 2000). According to the classification of Ishihara (1977), both porphyritic- and aplitic granites belong to the magnetite-series I-type granites (Fig. 10), indicating that these granites are highly oxidized and similar to those of typical porphyry Mo deposits. At Diyanqinamu, magnetite is widespread in K-feldspar ± magnetite and magnetite ± quartz hydrothermal mineral assemblages at the early stage. Locally, magnetite is also paragenetic with molybdenite (Fig. 6), suggesting that the hydrothermal fluids are also relatively oxidized at the early stage. Therefore, we inferred that the hydrothermal fluids in this deposit have inherited the highly oxidized signature of the granitic melts. High whole rock Fe_2O_3/FeO values, together with the occurrence of magnetite in hydrothermal mineral assemblages, point to the conclusion that the magmatic–hydrothermal systems at Diyanqinamu are highly oxidized.

Although there are some cases related to reduced systems such as the Baoguto Cu deposit (Cao et al., 2014) and Catface porphyry Cu (Mo–Au) deposit (Smith et al., 2012), most porphyry deposits are considered to have high oxygen fugacity (fO_2) (Rowins, 2000; Sun et al., 2013), with three important roles as follows. Firstly, melts with high fO_2 would have a greater capacity for sulfur (S) by substituting sulfide by sulfate as the major S-bearing phase, because the solubility of sulfide in magmas is generally lower than 1000 ppm, whereas that of sulfate could reach to ~9000 ppm or higher (Zhang et al., 2013). Secondly, more than 85% of S is present as sulfate in the melt with higher fO_2 (Jugo, 2009; Jugo et al., 2010), which yields much more S during partial

Table 5
The Mo contents of andesite in the Diyanqinamu deposit.
The Mo content in andesite is analyzed by ICP-MS in the State Key Laboratory of Ore Deposit Geochemistry in Guiyang. The analysis processes are described in detail by Qi and Gregoire (2000).

Lithology	Andesite											
	SHK3-1	SHK3-2	SHK3-3	SHK3-4	SHK3-5	SHK3-6	SHK3-7	SHK3-8	SHK3-9	SHK3-10	SHK3-11	SHK3-12
Mo (μg/g)	29.5	14.8	30.5	18.0	32.9	25.7	7.01	12.9	20.2	22.7	24.3	28.2

melting and eliminate residue sulfide in the source (Sun et al., 2004, 2013). Thirdly, the sulfide is kept undersaturated during the magma evolution because most S is present in the form of sulfate (Jugo et al., 2010; Mungall, 2002; Sun et al., 2004), which prevents the loss of S during magma evolution. Therefore, on one hand, the high fO_2 in the magma would facilitate sulfide mineralization afterward by supplying much more S. On the other hand, oxygen fugacity of the magma is important in controlling the compatibility for many ore-related elements in the magma (Blevin, 2004; Candela and Bouton, 1990). High fO_2 will enhance the Mo solubility, as demonstrated in previous experimental studies (Cao, 1989; Wood et al., 1987). Thus, the relatively high fO_2 of magmatic–hydrothermal system is also important for the Diyanqinamu Mo mineralization.

6.2.2. Fluorine contents of the granitic magma and their metallogenic significance

The discussion above indicates that the granites in this deposit are important sources for the Mo ore-forming minerals, but the question remains as whether these granites at Diyanqinamu can supply sufficient F for the widespread fluorite alteration. In general, halogen contents in igneous rocks are difficult to determine precisely because the magmas may experienced degassing during crystallization (Carmichael et al., 1974). Mica and apatite are important sinks for halogens and can be used to determine the F content in the magmas (Icenhower and London, 1997). As biotite is considered to be susceptible to subsolidus halogen exchange, apatite represents a better candidate for determining the F abundance in the magmas (Bath et al., 2013; Munoz, 1990; Piccoli et al., 1999) and is widely applied in porphyry Mo–(W) deposits to estimate the relative fugacities of F, Cl and OH (Cao et al., 2014; Gunow et al., 1980). Mineral chemical data show that apatite phenocrysts contain much high content of F (3.79–5.48 wt.%, avg. 4.53 wt.%) but lower Cl (0.01–0.05 wt.%, avg. 0.02 wt.%) content (Table 4 and Fig. 11). According to the partition coefficient of $D_{apatite/melt}$ (F) = 11–40 (Webster et al., 2009), the melt would theoretically contains

about 0.09–0.50 wt.% of F (Table 4). In contrast to Cl, fluorine content in magmas rises with fractional crystallization because of its incompatible element behavior (Aiuppa et al., 2009; Blevin and Chappell, 1992; Straub and Layne, 2003; Webster and De Vivo, 2002; Webster et al., 2009). Such high content of F is consistent with the nature that both porphyritic- and aplitic granites in this deposit are highly fractionated. Porphyritic granites with high F content are always associated with widespread fluorite alteration (Carten et al., 1988; McPhie et al., 2011; Mutschler et al., 1981; Wu et al., 2014), which is similar to the phenomenon observed at Diyanqinamu. It is worth noting that typical andesite around the world generally contains very low F content (http://georoc.mpch-mainz.gwdg.de/georoc/Start.asp), implying that the andesite at Diyanqinamu probably supply little F to the fluorite alteration. Consequently, fluorine is resulted mostly from the magmatic–hydrothermal fluid exsolution from the granitic melt, and the granites are characterized by very high content of F.

Although the partition behavior and transportation of Mo is independent of F (Tingle and Fenn, 1984), it is generally accepted that F is one of the most important volatiles in the magmas in reducing the magma viscosity (Baasner et al., 2013; Giordano et al., 2004; Schaller et al., 1992; Zimova and Webb, 2007), substantially lowering both the solidus and liquidus of the haplogranite system, causing a shift of the eutectic point towards more feldspar-rich compositions (Manning, 1981; Mysen et al., 2003), and increasing ion diffusivity in silicate melts (Giordano et al., 2004). The marked reduction in viscosity and density for F-rich granitic magmas would enhance various magmatic processes including partial melting, fractional crystallization and magma ascent (Taylor and Fallick, 1997), thereby leading to the Mo accumulation in the melt. In some cases, the intrusions associated with the porphyry Mo deposits are highly differentiated (Seedorff and Einaudi, 2004; White et al., 1981), such as ore-related intrusions in Henderson Mo mine (Gunow et al., 1980, Seedorff and Einaudi, 2004), Climax Mo mine (Cooke et al., 2005; Ludington and Plumlee, 2009), and Jiguanshan Mo mine (Wu et al., 2014). Therefore, F-rich magma
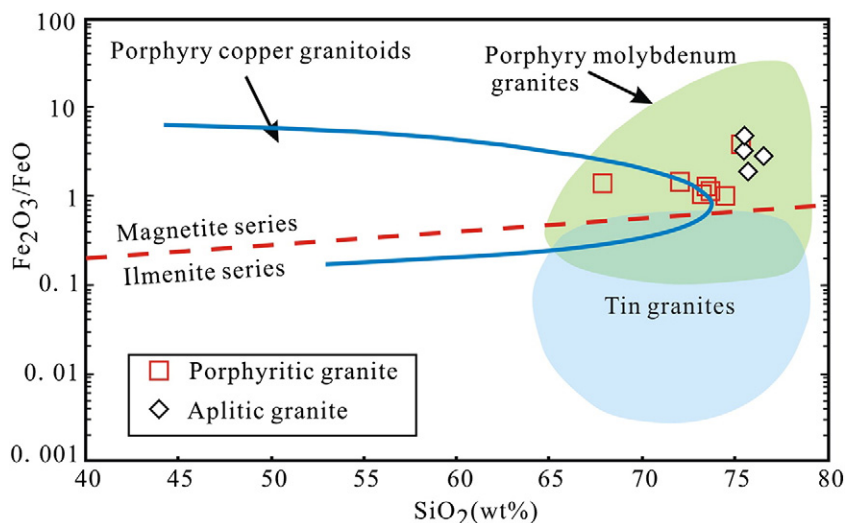

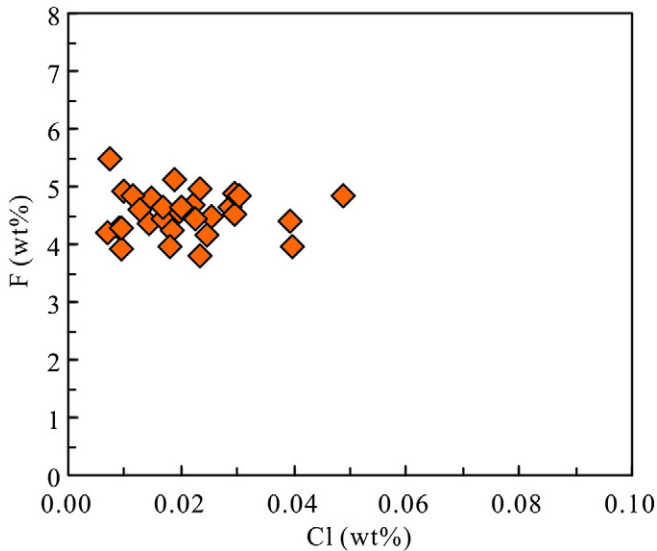Fig. 10. SiO_2 vs. Fe_2O_3/FeO plot of the porphyritic- and aplitic granites (Sinclair, 2007).

Fig. 11. Cl vs. F plot of apatite from the porphyritic granites.

plays an important role for the Mo mineralization in the Diyanqinamu deposit.

6.3. An integrated model and mineralization process

Based on existing and our new field observations, geochronological, isotopic (Sr, Nd and Pb isotopes) and mineral geochemical studies, we propose a genetic model for the Diyanqinamu porphyry Mo deposit, as discussed herein: In a post-collisional lithospheric extensional environment related to the closure of the Mongol–Okhotsk Ocean (Sun et al., 2014), highly felsic, oxidized and F-rich granitic magma derived from the partial melting of the pre-existing crustal components both "old" and "juvenile", intruded into the country rocks such as the Diyanqinamu andesite and volcaniclastic rocks. High-temperature, F-rich and high-fO_2 ore-bearing hydrothermal fluids may have fractionated from the highly differentiated granitic magma and underwent extensive circulation through the country rocks. During the hydrothermal circulations, the fluids have obtained some Mo from the ore-hosting andesite. Subsequently, the drop of oxygen fugacity by magnetite deposition and temperature has probably resulted in the formation of the Diyanqinamu Mo deposit.

7. Conclusions

Based on our new geological, geochronological, isotopic (Sr, Nd and Pb), and mineral geochemical evidence, we have reached the following conclusions:

(1) Although the intruding granites are barren, they represent important heat and ore-forming sources for the Diyanqinamu Mo deposit. In particular, the F from the granitic melts may have contributed to the widespread fluorite alteration.

(2) The andesite contains abnormally high Mo content. It is much older than the Mo mineralization, which indicates that the andesite may have only been a source of the ore-forming materials.

(3) The magmatic–hydrothermal system at Diyanqinamu is characterized by high fO_2 and F, which lay a foundation for the Mo mineralization. The drop of fO_2 and/or temperature may have probably resulted in the Mo mineralization.

References

Afshooni, S., Mirnejad, H., Esmaeily, D., Haroni, H.A., 2013. Mineral chemistry of hydrothermal biotite from the Kahang porphyry copper deposit (NE Isfahan), Central Province of Iran. Ore Geol. Rev. 54, 214–232.

Aiuppa, A., Baker, D.R., Webster, J.D., 2009. Halogens in volcanic systems. Chem. Geol. 263, 1–18.

Baasner, A., Schmidt, B.C., Webb, S.L., 2013. The effect of chlorine, fluorine and water on the viscosity of aluminosilicate melts. Chem. Geol. 357, 134–149.

Baker, J., Peate, D., Waight, T., Meyzen, C., 2004. Pb isotopic analysis of standards and samples using a [207]Pb–[204]Pb double spike and thallium to correct for mass bias with a double-focusing MC-ICP-MS. Chem. Geol. 211, 275–303.

Barker, S.L.L., Bennett, V.C., Cox, S.F., Norman, M.D., Gagan, M.K., 2009. Sm–Nd, Sr, C and O isotope systematics in hydrothermal calcite–fluorite veins: implications for fluid–rock reaction and geochronology. Chem. Geol. 268, 58–66.

Bath, A.B., Walshe, J.L., Cloutier, J., Verrall, M., Cleverley, J.S., Pownceby, M.I., Macrae, C.M., Wilson, N.C., Tunjic, J., Nortje, G.S., Robinson, P., 2013. Biotite and apatite as tools for tracking pathways of oxidized fluids in the Archean east repulse gold deposit, Australia. Econ. Geol. 108, 667–690.

Bau, M., Romer, R.L., Luders, V., Dulski, P., 2003. Tracing element sources of hydrothermal mineral deposits: REE and Y distribution and Sr–Nd–Pb isotopes in fluorite from MVT deposits in the Pennine Orefield, England. Miner. Depos. 38, 992–1008.

Belshaw, N.S., Freedman, P.A., O'Nions, R.K., Frank, M., Guo, Y., 1998. A new variable dispersion double-focusing plasma mass spectrometer with performance illustrated for Pb isotopes. Int. J. Mass Spectrom. 181, 51–58.

Blevin, P., 2004. Redox and compositional parameters for interpreting the granitoid metallogeny of eastern Australia: implications for gold-rich ore systems. Resour. Geol. 54, 241–252.

Blevin, P.L., Chappell, B.W., 1992. The role of magma sources, oxidation-states and fractionation in determining the granite metallogeny of eastern Australia. Trans. R. Soc. Edinb. Earth Sci. 83, 305–316.

Burnham, C.W., Ohmoto, H., 1980. Late-stage processes of felsic magmatism. In: Ishihara, S., Takenouchi, S. (Eds.), Granite Magmatism and Related Mineralization. Min. Geol. Spec. Issue 8, pp. 1–11.

Candela, P.A., 1997. A review of shallow, ore-related granites: textures, volatiles, and ore metals. J. Petrol. 38, 1619–1633.

Candela, P.A., Bouton, S.L., 1990. The influence of oxygen fugacity on tungsten and molybdenum partitioning between silicate melts and ilmenite. Econ. Geol. 85, 633–640.

Cao, X., 1989. Solubility of Molybdenite and the Transport of Molybdenum in Hydrothermal Solutions(Ph.D. Thesis) Iowa State University.

Cao, M.J., Qin, K.Z., Li, G.M., Jin, L.Y., Evans, N.J., Yang, X.R., 2014. Baogutu: an example of reduced porphyry Cu deposit in western Junggar. Ore Geol. Rev. 56, 159–180.

Carmichael, I.S.E., Turner, F.J., Verhoogen, J., 1974. Igneous Petrology. McGraw Hill, New York.

Carr, G.R., Dean, J.A., Suppel, D.W., Heithersay, P.S., 1995. Precise lead isotope fingerprinting of hydrothermal activity associated with Ordovician to Carboniferous metallogenic events in the Lachlan fold belt of New South Wales. Econ. Geol. 90, 1467–1505.

Carten, R.B., Geraghty, E.P., Walker, B.M., 1988. Cyclic development of igneous features and their relationship to high-temperature hydrothermal features in the Henderson porphyry molybdenum deposit, Colorado. Econ. Geol. 83, 266–296.

Castorina, F., Masi, U., Padalino, G., Palomba, M., 2008. Trace-element and Sr–Nd isotopic evidence for the origin of the Sardinian fluorite mineralization (Italy). Appl. Geochem. 23, 2906–2921.

Chang, Z.S., Meinert, L.D., 2004. The magmatic–hydrothermal transition—evidence from quartz phenocryst textures and endoskarn abundance in Cu–Zn skarns at the Empire Mine, Idaho, USA. Chem. Geol. 210, 149–171.

Chen, Y.J., Chen, H.Y., Zaw, K., Pirajno, F., Zhang, Z.J., 2007. Geodynamic settings and tectonic model of skarn gold deposits in China: an overview. Ore Geol. Rev. 31, 139–169.

Chen, B., Jahn, B.M., Tian, W., 2009. Evolution of the Solonker suture zone: constraints from zircon U–Pb ages, Hf isotopic ratios and whole-rock Nd–Sr isotope compositions of subduction and collision related magmas and forearc sediments. J. Asian Earth Sci. 34, 245–257.

Cooke, D.R., Hollings, P., Walshe, J.L., 2005. Giant porphyry deposits: characteristics, distribution, and tectonic controls. Econ. Geol. 100, 801–818.

Elburg, M.A., 1996. U–Pb ages and morphologies of zircon in microgranitoid enclaves and peraluminous host granites: evidence for magma mingling. Contrib. Mineral. Petrol. 123, 177–189.

Fan, W.M., Guo, F., Wang, Y.J., Lin, G., 2003. Late Mesozoic calc-alkaline volcanism of post-orogenic extension in the northern Da Hinggan Mountains, northeastern China. J. Volcanol. Geotherm. Res. 121, 115–135.

Giordano, D., Romano, C., Dingwell, D., Poe, B., Behrens, H., 2004. The combined effects of water and fluorine on the viscosity of silicic magmas. Geochim. Cosmochim. Acta 68, 5159–5168.

Gunow, A.J., Ludington, S., Munoz, J.L., 1980. Fluorine in micas from the Henderson molybdenite deposit, Colorado. Econ. Geol. 75, 1127–1137.

Guo, F., Fan, W., Gao, X., Li, C., Miao, L., Zhao, L., Li, H., 2010. Sr–Nd–Pb isotope mapping of Mesozoic igneous rocks in NE China: constraints on tectonic framework and Phanerozoic crustal growth. Lithos 120, 563–578.

Halliday, A.N., Shepherd, T.J., Dickiin, A.P., Chesley, J.T., 1990. Sm–Nd evidence for the age and origin of a Mississippi Valley Type ore deposit. Nature 344, 54–56.

Halter, W.E., Pettke, T., Heinrich, C.A., 2002. The origin of Cu/Au ratios in porphyry-type ore deposits. Science 296, 1844–1846.

Halter, W., Heinrich, C.A., Pettke, T., 2005. Magma evolution and the formation of porphyry Cu–Au ore fluids: evidence from silicate and sulfide melt inclusions. Miner. Depos. 39, 845–863.

Heinrich, C.A., Ryan, C.G., Mernagh, T.P., Eadington, P.J., 1992. Separation of ore metals between magmatic brine and vapor: a fluid inclusion study using PIXE microanalysis. Econ. Geol. 87, 1566–1583.

Hong, D.W., Wang, S.G., Xie, L.X., Zhang, J.S., Wang, T., 2003. Metallogenic province derived from mantle source: a case study of Central Asian Orogenic Belt. Miner. Depos. 22, 41–45 (in Chinese with English abstract).

Hoskin, P.W.O., Schaltegger, U., 2003. The composition of zircon and igneous and metamorphic petrogenesis. In: Hanchar, J.M., Hoskin, P.W.O. (Eds.), Zircon: Reviews in Mineralogy and Geochemistry. Miner. Soc. Am., pp. 27–62.

Hou, Z.Q., Yang, Z.M., 2009. Porphyry deposits in continental settings of China: geological characteristics, magmatic–hydrothermal system, and metallogenic model. Acta Geol. Sin. 83, 1779–1817 (in Chinese with English abstract).

Hu, Z.C., Liu, Y.S., Chen, L., Zhou, L., Li, M., Zong, K.Q., Zhu, L.Y., Gao, S., 2011. Contrasting matrix induced elemental fractionation in NIST SRM and rock glasses during laser ablation ICP-MS analysis at high spatial resolution. J. Anal. At. Spectrom. 26, 425–430.

Huang, D.H., 2007. Molybdenum deposit type and the geological and spatial–temporal evolution for the two major Mo deposit belts in China. The fifth seminar of geologic mapping and GIS, Geological Society of China, pp. 297–302 (in Chinese).

Huang, Z.L., Xu, C., Macaig, A., Liu, C.Q., Wu, J., Xu, D.R., Li, W.B., Guan, T., Xiao, H.Y., 2007. REE geochemistry of fluorite from the Maoniuping REE deposit, Sichuan Province, China: implications for the source of ore-forming fluids. Acta Geol. Sin. 81, 622–636.

Icenhower, J.P., London, D., 1997. Partitioning of fluorine and chlorine between biotite and granitic melt: experiment al calibration at 200 MPa H2O. Contrib. Mineral. Petrol. 127, 17–29.

Ishihara, S., 1977. The magnetite-series and ilmenite-series granitic rocks. Min. Geol. 27, 293–305.

Isozaki, Y., Aoki, K., Nakama, T., Yanai, S., 2010. New insight into a subduction-related orogen: a reappraisal of the geotectonic framework and evolution of the Japanese Islands. Gondwana Res. 18, 82–105.

Jackson, S.E., Pearson, N.J., Griffin, W.L., Belousova, E.A., 2004. The application of laser ablation-inductively coupled plasma-mass spectrometry to in situ U–Pb zircon geochronology. Chem. Geol. 211, 47–69.

Jahn, B.M., 2004. The Central Asian Orogenic Belt and growth of the continental crust in the Phanerozoic. Geol. Soc. Spec. Publ. 226, 73–100.

Jahn, B.M., Wu, F.Y., Chen, B., 2000. Granitoids of the Central Asian Orogenic Belt and continental growth in the Phanerozoic. Trans. R. Soc. Edinb. Earth Sci. 91, 181–193.

Jiang, G.Y., Quan, H., 1988. Mesozoic volcanic rocks of Genhe and Hailar basins in Da Hinggan Ling Range. Bull. Shenyang Inst. Res. Chin. Acad. Geol. Sci. 17, 23–100 (in Chinese with English abstract).

Jiang, Y., Ling, H., Jiang, S., Shen, W., Fan, H., Ni, P., 2006. Trace element and Sr–Nd isotope geochemistry of fluorite from the Xiangshan uranium deposit southeast China. Econ. Geol. 101, 1613–1622.

Jugo, P.J., 2009. Sulfur content at sulfide saturation in oxidized magmas. Geology 37, 415–418.

Jugo, P.J., Wilke, M., Botcharnikov, R.E., 2010. Sulfur K-edge XANES analysis of natural and synthetic basaltic glasses: implications for S speciation and S content as function of oxygen fugacity. Geochim. Cosmochim. Acta 74, 5926–5938.

Kinnaird, J.A., Kruger, F.J., Cawthorn, R.G., 2004. Rb–Sr and Nd–Sm isotopes in fluorite related to the granites of the Bushveld Complex. S. Afr. J. Geol. 107, 413–430.

Kröner, A., Liu, D., 2012. Advances in high-resolution ion-microprobe geochronology. Gondwana Res. 21, 717–718.

Leng, C.B., Zhang, X.C., Huang, Z.L., Huang, Q.Y., Wang, S.X., Ma, D.Y., Luo, T.Y., Li, C., Li, W.B., 2014. Geology, Re–Os ages, sulfur and lead isotopes of the Diyanqinamu Porphyry Mo deposit, Inner Mongolia, NE China. Econ. Geol. (accepted for publication).

Li, J.Y., 2006. Permian geodynamic setting of Northeast China and adjacent regions: closure of the Paleo-Asian Ocean and subduction of the Paleo-Pacific Plate. J. Asian Earth Sci. 26, 207–224.

Li, K., Zhang, Z.C., Li, J.F., Tang, W.H., Feng, Z.S., Li, Q.G., 2012. Zircon SHRIMP U–Pb age and geochemical characteristics of the Mesozoic volcanic rocks in Xi Ujimqin Banner, Inner Mongolia. Geol. Bull. Chin. 31, 671–685 (in Chinese with English abstract).

Liu, Y.S., Gao, S., Hu, Z.C., Gao, C.G., Zong, K.Q., Wang, D.B., 2010a. Continental and oceanic crust recycling-induced melt–peridotite interactions in the Trans-North China Orogen: U–Pb dating, Hf isotopes and trace elements in zircons from mantlexenoliths. J. Petrol. 51, 537–571.

Liu, Y.S., Hu, Z.C., Zong, K.Q., Gao, C.G., Gao, S., Xu, J., Chen, H.L., 2010b. Reappraisement and refinement of zircon U–Pb isotope and trace element analyses by LA-ICP-MS. Chin. Sci. Bull. 55, 1535–1546 (in Chinese).

Loferski, P.J., Ayuso, R.A., 1995. Petrography and mineral chemistry of the composite Deboullie pluton, northern Maine, U.S.A.: implications for the genesis of Cu Mo mineralization. Chem. Geol. 123, 89–105.

Lowenstern, J.B., Sinclair, W.D., 1996. Exsolved magmatic fluid and its role in the formation of comb-layered quartz at the cretaceous Logtung W–Mo deposit, Yukon Territory, Canada. Trans. R. Soc. Edinb. Earth Sci. 87, 291–303.

Ludington, S., Plumlee, G.S., 2009. Climax-type porphyry molybdenum deposits. U.S. Geol. Surv. Open-File Rep., pp. 1–16.

Manning, D., 1981. The effect of fluorine on liquidus phase relationships in the system Qz–Ab–Or with excess water at 1 kb. Contrib. Mineral. Petrol. 76, 206–215.

Maruyama, S., Send, T., 1986. Orogeny and relative plate motions: example of the Japanese Islands. Tectonophysics 127, 305–329.

McPhie, J., Kamenetsky, V., Allen, S., Ehrig, K., Agangi, A., Bath, A., 2011. The fluorine link between a supergiant ore deposit and a silicic large igneous province. Geology 39, 1003–1006.

Meng, Q.R., 2003. What drove late Mesozoic extension of the northern China–Mongolia tract? Tectonophysics 369, 155–174.

Metelkin, D.V., Gordienko, I.V., Klimuk, V.S., 2007. Paleomagnetism of Upper Jurassic basalts from Transbaikalia: new data on the time of closure of the Mongol–Okhotsk Ocean and Mesozoic intraplate tectonics of Central Asia. Russ. Geol. Geophys. 48, 825–834.

Metelkin, D.V., Vernikovsky, V.A., Kazansky, A.Y., Wingate, M.T.D., 2010. Late Mesozoic tectonics of Central Asia based on paleomagnetic evidence. Gondwana Res. 18, 400–419.

Mountain, B.W., Seward, T.M., 1999. The hydrosulfide/sulfide complexes of copper (I): Experimental determination of stoichiometry and stability at 22 °C and reassessment of high temperature data. Geochim. Cosmochim. Acta 63, 11–29.

Mountain, B.W., Seward, T.M., 2003. Hydrosulfide/sulfide complexes of copper (I): experimental confirmation of the stoichiometry and stability of $Cu(HS)_2^{2-}$ to elevated temperatures. Geochim. Cosmochim. Acta 67, 3005–3014.

Mungall, J.E., 2002. Roasting the mantle: slab melting and the genesis of major Au and Au-rich Cu deposits. Geology 30, 915–918.

Munoz, J.L., 1984. F–OH and Cl–OH exchange in micas with applications to hydrothermal ore deposits. In micas. Rev. Mineral. Geochem. 13, 469–493.

Munoz, J.L., 1990. F and Cl contents of hydrothermal biotites: a reevaluation. Geol. Soc. Am. 22, 135.

Mutschler, F.E., Wright, E.G., Ludington, S., Abbott, J.T., 1981. Granite molybdenite systems. Econ. Geol. 76, 874–897.

Mysen, B.O., Cody, G.D., Smith, A., 2003. Solubility mechanisms of fluorine in peralkaline and meta-aluminous silicate glasses and in melts to magmatic temperatures. Geochim. Cosmochim. Acta 68, 2745–2769.

Nachit, H., Ibhi, A., Abia, E.H., Ben Ohoud, M., 2005. Discrimination between primary magmatic biotites, reequilibrated biotites and neoformed biotites. C. R. Geosci. 337, 1415–1420.

Nie, X.L., Hou, W.R., 2010. The discovery of the Diyanqinamu large-size Mo–Ag deposit, Inner Mongolia, and its geological significance. Acta Geosci. Sin. 31, 469–472 (in Chinese with English abstract).

Nie, F.J., Jiang, S.H., Zhang, Y., Liu, Y., Hu, P., 2004. Geological features and origin of porphyry copper deposits in China–Mongolia border region and its neighboring area. Miner. Depos. 23, 176–189 (in Chinese with English abstract).

Nie, F.J., Jiang, S.H., Zhang, Y., Bai, D.M., Hu, P., Zhao, Y.Y., Zhang, W.Y., Liu, Y., 2007. Metallogenic Studies and Prospecting Orientation in Central and Eastern Segments Along China–Mongolia Border. Geological Publishing House, Beijing, p. 195 (in Chinese with English abstract).

Pettke, T., Oberli, F., Heinrich, C.A., 2010. The magma and metal source of giant porphyry-type ore deposits, based on lead isotope microanalysis of individual fluid inclusions. Earth Planet. Sci. Lett. 296, 267–277.

Piccoli, P.M., Candela, P.A., Williams, T.J., 1999. Estimation of aqueous HCl and Cl concentrations in felsic systems. Lithos 46, 591–604.

Qi, L., Gregoire, D.C., 2000. Determination of trace elements in twenty six Chinese geochemistry reference materials by inductively coupled plasma-mass spectrometry. Geostand. Newslett. 24, 51–63.

Ratajeski, K., 1995. Estimation of Initial and Saturation Water Concentration for Three Granitic Plutons in the North-Central Great Basin, Nevada. University of Maryland, College Park.

Ren, J., Tamaki, K., Li, S., Junxia, Z., 2002. Late Mesozoic and Cenozoic rifting and its dynamic setting in Eastern China and adjacent areas. Tectonophysics 344, 175–205.

Rowins, S.M., 2000. Reduced porphyry copper–gold deposits: a new variation on an old theme. Geology 28, 491–494.

Sanchez, V., Cardellach, E., Corbella, M., Vindel, E., Martin-Crespo, T., Boyce, A.J., 2010. Variability in fluid sources in the fluorite deposits from Asturias (N Spain): further evidences from REE, radiogenic (Sr, Sm, Nd) and stable (S, C, O) isotope data. Ore Geol. Rev. 37, 87–100.

Schaller, T., Dingwell, D.B., Keppler, H., Knöller, W., Merwin, L., Sebald, A., 1992. Fluorine in silicate glasses: a multinuclear nuclear magnetic resonance study. Geochim. Cosmochim. Acta 56, 701–707.

Seedorff, E., Einaudi, M.T., 2004. Henderson porphyry molybdenum system, Colorado: I. Sequence and abundance of hydrothermal mineral assemblages, flow paths of evolving fluids, and evolutionary style. Econ. Geol. 99, 3–37.

Seedorff, E., Dilles, J., Proffett, J., Einaudi, M., Zurcher, L., Stavast, W., Johnson, D., Barton, M., 2005. Porphyry deposits: characteristics and origin of hypogene features. Econ. Geol. 100th Anniversary 29, pp. 251–298.

Sengör, A.M.C., Natal'in, B.A., 1996. Paleotectonics of Asia: fragments of a synthesis. In: Yin, A., Harrison, M. (Eds.), The Tectonic Evolution of Asia. Cambridge University Press, pp. 486–640.

Seward, T.M., Barnes, H.L., 1997. Metal transport by hydrothermal ore fluids. In: Barnes, H. L. (Ed.), Geochemistry of Hydrothermal Ore Deposits. John Wiley and Sons, New York, pp. 435–486.

Shandong Gold Group Co. LTD., 2012. Geological survey report of Diyanqinamu Mo polymetallic ore deposit of Inner Mongolia, China.

Shao, J.A., Zhang, L.Q., Mou, B.L., 2011. Distribution of uranium and molybdenum deposits and their relationship with medium massifs in Central Asian Orogenic Zone. J. Jilin Univ. (Earth Sci. Ed.) 41, 1667–1675 (in Chinese with English abstract).

Shen, W.J., Wang, X.Q., Nie, L.S., 2012. Regional geochemical indicators of large-sized silver polymetallic deposits in Daxing'anling Metallogenic Belt. Front. Earth Sci. 19, 049–058 (in Chinese with English abstract).

Sinclair, W., 2007. Porphyry deposits. Mineral deposits of Canada: a synthesis of major deposit-types, district metallogeny, the evolution of geological provinces, and exploration methods. Geo. Assoc. Can., Miner. Depos. Div. Spec. Publ. 5, pp. 223–243.

Sláma, J., Košler, J., Condon, D.J., Crowley, J.L., Gerdes, A., Hanchar, J.M., Horstwood, M.S., Morris, G.A., Nasdala, L., Norberg, N., 2008. Plešovice zircon—a new natural reference material for U–Pb and Hf isotopic microanalysis. Chem. Geol. 249, 1–35.

Smith, C.M., Canil, D., Rowins, S.M., Friedman, R., 2012. Reduced granitic magmas in an arc setting: the Catface porphyry Cu–Mo deposit of the Paleogene Cascade Arc. Lithos 154, 361–373.

Straub, S.M., Layne, G.D., 2003. The systematics of chlorine, fluorine, and water in Izu arc front volcanic rocks: implications for volatile recycling in subduction zones. Geochim. Cosmochim. Acta 67, 4179–4203.

Sun, W.D., Arculus, R.J., Kamenetsky, V.S., Binns, R.A., 2004. Release of gold-bearing fluids in convergent margin magmas prompted by magnetite crystallization. Nature 431, 975–978.

Sun, X., Deng, J., Yang, L.Q., Wang, Q.F., Yang, Z.R., Gong, Q.J., Wang, C.M., 2010. REE and Sr–Nd isotope geochemistry for Yixian fluorite deposit, Western Liaoning Province, China, and its geological implications. J. Earth Sci. 21, 227–235.

Sun, W.D., Liang, H.Y., Ling, M.X., Zhan, M.Z., Ding, X., Zhang, H., Yang, X.Y., Li, Y.L., Ireland, T.R., Wei, Q.R., Fan, W.M., 2013. The link between reduced porphyry copper deposits and oxidized magmas. Geochim. Cosmochim. Acta 103, 263–275.

Sun, H.R., Huang, Z.L., Li, W.B., Leng, C.B., Ma, D.Y., Zhang, X.C., 2014. Chronology, geochemistry and Sr–Nd isotope studies of Jurassic intrusions in the Diyanqinamu porphyry Mo mine, central Inner Mongolia, China. J. Asian Earth Sci. http://dx.doi.org/10.1016/j.jseaes.2014.03.014.

Taylor, R.P., Fallick, A.E., 1997. The evolution of fluorine-rich felsic magmas: source dichotomy, magmatic convergence and the origins of topaz granite. Terra Nova 9, 105–108.

Tingle, T.N., Fenn, P.M., 1984. Transport and concentration of molybdenum in granite molybdenite systems: effects of fluorine and sulfur. Geology 12, 156–158.

Tomurtogoo, O., Windley, B.F., Kroner, A., Badarch, G., Liu, D.Y., 2005. Zircon age and occurrence of the Adaatsag ophiolite and Muron shear zone, central Mongolia: constraints on the evolution of the Mongol–Okhotsk Ocean, suture and orogen. J. Geol. Soc. 162, 125–134.

Utsunomiya, A., Suzuki, N., Ota, T., 2008. Preserved paleo-oceanic plateaus in accretionary complexes: implications for the contributions of the Pacific superplume to global environmental change. Gondwana Res. 14, 115–125.

Wang, F., Zhou, X.H., Zhang, L.C., Ying, J.F., Zhang, Y.T., Wu, F.Y., Zhu, R.X., 2006. Late Mesozoic volcanism in the Great Xing'an Range (NE China): timing and implications for the dynamic setting of NE Asia. Earth Planet. Sci. Lett. 251, 179–198.

Wang, T., Jahn, B.M., Kovach, V.P., Tong, Y., Hong, D.W., Han, B.F., 2009. Nd–Sr isotopic mapping of the Chinese Altai and implications for continental growth in the Central Asian Orogenic Belt. Lithos 110, 359–372.

Webster, J.D., De Vivo, B., 2002. Experimental and modeled solubilities of chlorine in aluminosilicate melts, consequences of magma evolution, and implications for exsolution of hydrous chloride melt at Mt Somma-Vesuvius. Am. Mineral. 87, 1046–1061.

Webster, J.D., Tappen, C.M., Mandeville, C.W., 2009. Partitioning behavior of chlorine and fluorine in the system apatite–melt–fluid. II: Felsic silicate systems at 200 MPa. Geochim. Cosmochim. Acta 73, 559–581.

White, W., Bookstrom, A., Kamilli, R., Ganster, M., Smith, R., Ranta, D., Steininger, R., 1981. Character and origin of Climax-type molybdenum deposits. Econ. Geol. 75, 270–316.

Wiedenbeck, M., AllÉ, P., Corfu, F., Griffin, W.L., Meier, M., Oberli, F., Quadt, A.V., Roddick, J. C., Spiegel, W., 1995. Three natural zircon standards for U–Th–Pb, Lu–Hf, trace element and REE analyses. Geostand. Newslett. 19, 1–23.

Williams-Jones, A.E., Heinrich, C.A., 2005. 100th anniversary special paper: vapor transport of metals and the formation of magmatic–hydrothermal ore deposits. Econ. Geol. 100, 1287–1312.

Wood, S.A., Crerar, D.A., Borcsik, M.P., 1987. Solubility of the assemblage pyrite–pyrrhotite–magnetite–sphalerite–galena–Au–stibnite–bismuthinite–argentite–molybdenite in H$_2$O–CO$_2$–NaCl solutions from 200 to 350 °C. Econ. Geol. 82, 1864–1887.

Wu, F.Y., Jahn, B.M., Wilde, S.A., Sun, D.Y., 2000. Phanerozoic crustal growth: U–Pb and Sr–Nd isotopic evidence from the granites in northeastern China. Tectonophysics 328, 89–113.

Wu, F.Y., Jahn, B.M., Wilde, S.A., Lo, C.H., Yui, T.F., Lin, Q., Ge, W.C., Sun, D.Y., 2003. Highly fractionated I-type granites in NE China (II): isotopic geochemistry and implications for crustal growth in the Phanerozoic. Lithos 67, 191–204.

Wu, F.Y., Lin, J.Q., Wilde, S.A., Zhang, X.O., Yang, J.H., 2005. Nature and significance of the Early Cretaceous giant igneous event in eastern China. Earth Planet. Sci. Lett. 233, 103–119.

Wu, F.Y., Yang, J.H., Lo, C.H., Wilde, S.A., Sun, D.Y., Jahn, B.M., 2007. Jiamusi Massif in China: a Jurassic accretionary complex in the western Pacific margin. Isl. Arc 16, 156–172.

Wu, H.Y., Zhang, L.C., Chen, Z.G., Wan, B., Xiang, P., Zhang, X.J., 2010. Hypersaline, high-oxygen fugacity and F-rich fluid inclusions in Jiguanshan porphyry molybdenum deposit, Xilamulun metallogenic belt. Acta Petrol. Sin. 26, 1363–1374.

Wu, F.Y., Sun, D.Y., Ge, W.C., Zhang, Y.B., Grant, M.L., Wilde, S.A., Jahn, B.M., 2011. Geochronology of the Phanerozoic granitoids in northeastern China. J. Asian Earth Sci. 41, 1–30.

Wu, H.Y., Zhang, L.C., Pirajno, F., Xiang, P., Wan, B., Chen, Z.G., Xiang, P., Zhang, X.J., 2014. The Jiguanshan porphyry Mo deposit in the Xilamulun metallogenic belt, northern margin of the North China Craton, U–Pb geochronology, isotope systematics, geochemistry and fluid inclusion studies: implications for a genetic model. Ore Geol. Rev. 56, 549–565.

Xiao, W.J., Windley, B.F., Hao, J., Zhai, M.G., 2003. Accretion leading to collision and the Permian Solonker suture, Inner Mongolia, China: termination of the central Asian orogenic belt. Tectonics 22.

Xu, W.L., Pei, F.P., Wang, F., Meng, E., Ji, W.Q., Yang, D.B., Wang, W., 2013. Spatial–temporal relationships of Mesozoic volcanic rocks in NE China: constraints on tectonic overprinting and transformations between multiple tectonic regimes. J. Asian Earth Sci. 74, 167–193.

Xue, H.M., Guo, L.J., Hou, Z.Q., Zhou, X.W., Tong, Y., Pan, X.F., 2009. The Xilingele complex from the eastern part of the Central Asian Orogenic Belt, China: products of early Variscan orogeny other than ancient block: evidence from zircon SHRIMP U–Pb ages. Acta Petrol. Sin. 25, 2001–2010 (in Chinese with English abstract).

Yan, H., Huang, F.X., Sun, H., Zhao, L.Q., Zhang, Y., Zhang, H., Li, S.Z., Liu, F.F., Wang, J.S., 2012. A model for alteration zoning of hydrothermal mineralization based on Surpac software for the Diyanqinamu Mo mine district, Inner Mongolia. Geol. Explor. 48, 932–939 (in Chinese with English abstract).

Ying, J.F., Zhou, X.H., Zhang, L.C., Wang, F., 2010. Geochronological framework of Mesozoic volcanic rocks in the Great Xing'an Range, NE China, and their geodynamic implications. J. Asian Earth Sci. 39, 786–793.

Zartman, R.E., Doe, B.R., 1981. Plumbotectonics — the model. Tectonophysics 75, 135–162.

Zhang, J.H., Ge, W.C., Wu, F.Y., Wilde, S.A., Yang, J.H., Liu, X.M., 2008a. Large-scale Early Cretaceous volcanic events in the northern Great Xing'an Range, Northeastern China. Lithos 102, 138–157.

Zhang, L.C., Zhou, X.M., Ying, J.F., Wang, F., Guo, F., Wan, B., Chen, Z.G., 2008b. Geochemistry and Sr–Nd–Pb–Hf isotopes of Early Cretaceous basalts from the Great Xinggan Range, NE China: implications for their origin and mantle source characteristics. Chem. Geol. 256, 12–23.

Zhang, W.Y., Nie, F.J., Jiang, S.H., Liu, Y., Hu, P., Xu, D.Q., Cui, X.M., Bai, D.M., 2009. Magmatic Activity and Metallogeny of Dong Ujimqin Banner, Inner Mongolia. Geological Publishing House, Beijing, pp. 1–128 (in Chinese with English abstract).

Zhang, J.H., Gao, S., Ge, W.C., Wu, F.Y., Yang, J.H., Wilde, S.A., Li, M., 2010. Geochronology of the Mesozoic volcanic rocks in the Great Xing'an Range, northeastern China: implications for subduction-induced delamination. Chem. Geol. 276, 144–165.

Zhang, F.Q., Chen, H.L., Yu, X., Dong, C.W., Yang, S.F., Pang, Y.M., Batt, G.E., 2011. Early Cretaceous volcanism in the northern Songliao Basin, NE China, and its geodynamic implication. Gondwana Res. 19, 163–176.

Zhang, H., Ling, M.X., Liu, Y.L., Tu, X.L., Wang, F.Y., Li, C.Y., Liang, H.Y., Yang, X.Y., Arndt, N.T., Sun, W.D., 2013. High oxygen fugacity and slab melting linked to Cu mineralization: evidence from Dexing porphyry copper deposits, Southeastern China. J. Geol. 121, 289–305.

Zhou, C.X., Wei, C.S., Guo, J.Y., Li, C.Y., 2001. The source of metals in the Qilinchang Zn–Pb deposit, northeastern Yunnan, China: Pb–Sr isotope constraints. Econ. Geol. 96, 583–598.

Zhou, J.B., Wilde, S.A., Zhang, X.Z., Zhao, G.C., Zheng, C.Q., Wang, Y.J., Zhang, X.H., 2009. The onset of Pacific margin accretion in NE China: evidence from the Heilongjiang high-pressure metamorphic belt. Tectonophysics 478, 230–246.

Zhou, J.X., Huang, Z.L., Zhou, M.F., Li, X.B., Jin, Z.G., 2013. Constraints of C–O–S–Pb isotope compositions and Rb–Sr isotopic age on the origin of the Tianqiao carbonate-hosted Pb–Zn deposit, SW China. Ore Geol. Rev. 53, 77–92.

Zimova, M., Webb, S.L., 2007. The combined effects of chlorine and fluorine on the viscosity of aluminosilicate melts. Geochim. Cosmochim. Acta 71, 1553–1562.

Zonenshain, L., Kuzmin, M., Natapov, L., 1990. Geology of USSR: a plate tectonic synthesis. American Geophysics Union, Geodynamic Series 21, p. 242.